Please cite the Published Version

Goudar, Dayanand M., Khaji, Saiyad Hasan, Haider, Julfikar , Sherwin, Canute, Bhat, Subraya Krishna, Jagadeesha, T and Raju, K (2025) Influence of Titanium on the Microstructure and Wear Properties of Spray-Formed Hypereutectic Al-Si Alloys. Journal of Materials Engineering and Performance. ISSN 1059-9495

DOI: https://doi.org/10.1007/s11665-025-11759-5

Publisher: Springer

Version: Accepted Version

Downloaded from: https://e-space.mmu.ac.uk/641608/

Usage rights: (cc) BY Creative Commons: Attribution 4.0

Enquiries:

If you have questions about this document, contact openresearch@mmu.ac.uk. Please include the URL of the record in e-space. If you believe that your, or a third party's rights have been compromised through this document please see our Take Down policy (available from https://www.mmu.ac.uk/library/using-the-library/policies-and-guidelines)

Influence of Titanium on the Microstructure and Wear Properties of Spray-Formed Hypereutectic Al-Si Alloys

Dayanand M. Goudar^{a*}, Saiyad Hasan Khaji^a, Julfikar Haider^b, Canute Sherwin^c, Subraya Krishna Bhat^d, Jagadeesha. T^e, K. Raju^f

^aDepartment of Mechanical Engineering, Tontadarya College of Engineering, Gadag-582101, India

^bDepartment of Engineering, Manchester Metropolitan University, Manchester, UK

^cCoE – Energy Science and e-Mobility, Atria University, Karnataka –560 024, India

^dDepartment of Mechanical and Industrial Engineering, MIT, MAHE, Manipal–576104, India

^eDepartment of Mechanical Engineering, National Institute of Technology, Kozhikode–673601, India

^fDepartment of Mechanical Engineering, St. Joseph Engineering College, Mangaluru–575028, India

^{*}Corresponding Author, e- mail: <u>dayanand_goudar@yahoo.co.in</u>

Abstract: The present study explored the development of hypereutectic Al-Si alloys such as Al-15Si (SF1), Al-15Si-0.5Ti (SF2), Al-15Si-1.0Ti (SF3), and Al-15Si-2Ti (SF4) alloys by spray forming, a technique that yields refined microstructures with minimal segregation, and examined the effects of titanium (Ti) on the microstructure and wear properties of alloys at various temperatures. Microstructural analysis revealed equiaxed aluminum (Al) matrices with distributed silicon (Si) phases and Al₃Ti intermetallics in Ti-containing alloys. The addition of Ti refined the microstructure and enhanced the refinement of Si particles. The hardness increased as Ti content increased in the alloy, with spray-formed alloys (SF) exhibiting 30–35% higher hardness than their as-cast (AC) counterparts at all temperatures. The SF alloys demonstrated improved wear resistance, with 50-65% lower wear rates than AC alloys at 25°C and 68-82% lower at 250°C. Specifically, the Al-15Si-2Ti SF alloy exhibited 62% and 82% lower wear rates than Al-15Si-2TiAC alloy at 25°C and 250°C respectively. The coefficient of friction (COF) decreased with load for both AC and SF alloys, while COF values increased as the temperature increased. The AC alloys exhibited a 21-35% increase in coefficient of friction (µ) per unit rise in temperature, while SF alloys showed a significantly lower increase of 0.18-0.29%. The SF4 alloy demonstrated the lowest COF across the entire load and temperature range. Spray-formed hypereutectic Al-Si-Ti alloys demonstrate a high potential for aerospace and automotive applications due to their refined microstructure and enhanced wear resistance, achieved through addition of Ti, making them suitable for high-performing applications.

Keywords: Al-Si-Ti alloys, Spray forming, Microstructure, Hardness, Tribology

1. Introduction

To increase energy efficiency and sustainability, the aerospace and automotive sectors are shifting toward adopting lightweight materials. Aluminum alloys are promising substitutes for cast iron and steel because of their low density and high specific stiffness [1]. Al-Si alloys excel in large-scale applications because of their exceptional combination of low density, high performance, and excellent durability. Moreover, increasing the silicon content beyond the eutectic composition enhances a range of critical properties, including wear resistance, fluidity, machinability, high-temperature resistance, modulus of elasticity, hardness, and stiffness. In hypereutectic Al-Si alloys, the primary Si crystal size, morphology, and distribution dictate wear behavior, whereas the optimized Si content, microstructure, and mechanical properties make them ideal for demanding applications requiring weight reduction and enhanced performance.

Conventionally cast hypereutectic Al-Si alloys form coarse microstructures with blocks such as primary Si, needle-like eutectic Si, and dendritic matrices that degrade machinability, mechanical properties, and wear resistance [3]. Al-Si alloys with fine, homogeneous primary Si and eutectic phases demonstrate exceptional strength and excellent wear resistance [4]. Copper (Cu) and magnesium (Mg) in Al-Si alloys increase their mechanical strength; however, the increase in wear resistance is limited to temperatures below 200°C. At higher temperatures, traditional intermetallic phases such as Mg₂Si, Q-Al-Mg-Si-Cu, and θ-Al₂Cu rapidly coarsen above 200°C, resulting in poor wear performance [5]. The addition of transition metals and rare-earth elements, such as Zr, Ti, Sc, and V, to Al-Si alloys can improve their high-temperature wear performance through the formation of heat-resistant precipitates in the microstructure. These transition elements have limited solubility and mobility in the Al matrix, preserving the original solidification microstructure of the Al alloy upon cooling [6]. It has been demonstrated that adding titanium (Ti) to Al-Si alloys improves their resistance to wear at high temperatures [7]. Strong intermetallic phases and a modified microstructure that results in greater hardness and less vulnerability to brittle delamination improving the wear resistance [8]. The solubility limit of Ti in Al is between 0.12% and 0.15 wt. %, which is the typical level used in grain-refined Al-Si alloys. However, excessive Ti can cause problems in the liquid metal process and defects in casting because of the precipitation of the primary coarse Ti-Al-Si. The addition of Ti to the binary hypereutectic Al-Si alloy led to the precipitation of Al₃Ti and Ti-Al-Si intermetallic phases at sufficiently high levels. According to previous reports, the morphology of Ti-Al-Si intermetallics in Al-Si foundry alloys, such as flakes and blocks, is on par with that of Al₃Ti in binary alloys [9]. Zeren and Karakulak analyzed the microstructural characteristics and tribological properties of Al–Six–Ti cast alloys [10].

Studies have revealed that the addition of Ti to Al-Si alloys results in the precipitation of the Ti-Al-Si intermetallic phase [11]. Increasing the Ti content increases the hardness and wear resistance due

to the increasing volume fraction of relatively hard intermetallic compounds. Ghomashchi [12] reported that rapid solidification cooling and a lower Ti content in A356 Al alloys favored the formation of flake-like Ti-based intermetallics, whereas slower cooling and increased Ti content resulted in the development of a blocky microstructure. Zeren et al. examined the influence of Ti addition on the microstructural and hardness properties of near-eutectic Al–Si alloys. According to their findings, the development of hard Al₃Ti intermetallics caused the Ti-Al-Si particles to coarsen, and the hardness significantly increased as the Ti content increased from 0.1% to 10%. The hardness increased from 841 to 1543 HV [13].

Gao et al. examined the influence of Si and Ti addition on the properties of Ti-Al-Si intermetallics. Their findings indicated that a higher Si content led to improved microhardness and the formation of Ti-Al-Si intermetallics with a flake-like morphology, characterized by increased Si content. However, the addition of Ti to Al-Si alloys results in microstructural modification, improved wear resistance, and enhanced friction performance, thereby substantially enhancing their overall tribological properties [14]. Saheb et al. examined the effect of Ti addition (up to 4 wt.%) on the wear properties of rapidly solidified 12% Si eutectic alloys, both cast and heat-treated. Their research revealed that the presence of Al₃Ti, a moderately hard phase, substantially enhanced the microhardness of Ti-containing alloys, leading to improved wear resistance and reduced susceptibility to wear damage. Furthermore, they reported that adding 2–3 wt.% Ti to the alloys resulted in optimal wear performance [15]. Xie et al. explored the connection between wear resistance and yield strength in Al-Si-Ti piston alloys by analyzing the wear mechanism through elastic contact theory. Their findings revealed that the wear resistance of the Al-Si-Ti alloy was 150% greater than that of the Al-Si alloy, with the primary wear mechanism being plastic deformation wear [16]. Subhi et al. investigated the tribological behavior of hypoeutectic Al-7Si alloys with various Ti contents (0.8–1.6%) under dry sliding conditions. This study revealed that the addition of Ti to Al-Si alloys resulted in a significant increase in the alloy hardness, which was attributed to the formation of Al₃Ti, which in turn led to a substantial decrease in the wear rate as the Ti content increased [17]. Kim et al. reported that the Al-12Si-2.3Ti-1B alloy exhibited the highest hardness and lowest wear rate compared with those of other Al-Si alloys due to the presence of the strengthening phases Al₃Ti and (Al-Ti) B₂, which enhanced its mechanical properties and wear resistance [18].

A critical literature survey revealed that research has focused primarily on the role of Ti in refining Al–Si grains via the conventional casting route to enhance their mechanical properties, with few studies exploring the impact of Ti on the wear behavior of Al–Si alloys at room temperature. Hypereutectic Al-Si-Ti alloys have traditionally been processed through casting, but this route leads to coarse microstructures consisting of large silicon grains and flake-like Ti intermetallic phases,

which compromise wear properties and machinability. Spray-forming, which is a rapid solidification process, has emerged as a promising alternative, yielding superior mechanical, wear, and corrosion properties of alloys owing to microstructural refinement and extended solid solubility limits overcoming conventional ingot metallurgy limitations. Numerous studies have been carried out to explore the impact of the spray forming process on the refinement of the silicon phase in hypereutectic Al-Si alloys [19]. Research by Gupta and Lavernia demonstrated a significant reduction in the silicon phase in a hypereutectic Al-Si alloy compared to its cast counterpart [20]. Additionally, Grant reported that the spray forming process not only refines the microstructure but also enhances the solid solubility, leading to improved tribological properties of hypereutectic Al-Si alloys [21]. No work has been reported in the literature on the wear behavior of spray-formed Al-Si-Ti alloys, especially at elevated temperatures. The present study has focused on investigating the tribological properties of spray-formed hypereutectic Al-15Si-Ti alloys with varying amounts of Ti (0.0 to 2.0 wt. %) at room temperature as well as at elevated temperatures, (25°C to 250°C) and benchmarking them against their conventionally cast counterparts.

2. Materials and methods

2.1. Alloy compositions and cast sample preparation

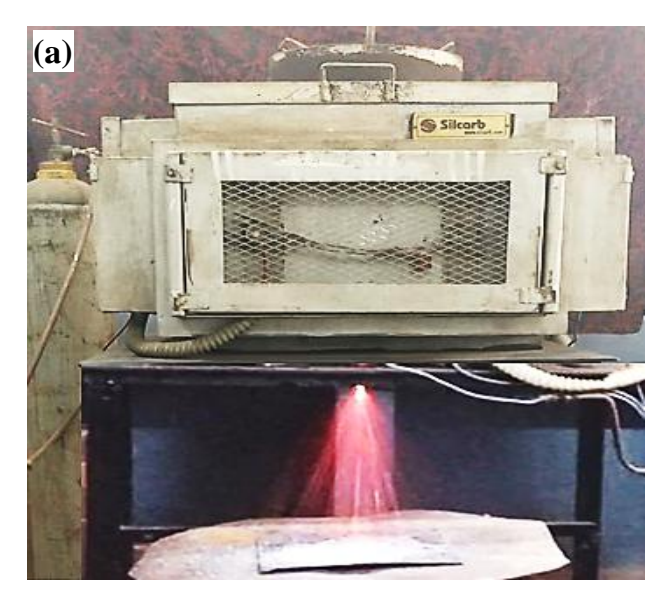
The hypereutectic Al-15Si (AC1), Al-15Si-0.5Ti (AC2), Al-15Si-1.0Ti (AC3), and Al-15Si-2.0Ti (AC4) alloys were sourced from Fenfee Metallurgicals, India. These alloys were produced through a controlled melting process, utilizing pure aluminum along with master alloys to achieve the desired chemical compositions. Al-25Si and Al-5Ti master alloys were used as the sources of silicon and titanium, respectively. During alloy preparation, pure aluminum was first charged into a resistance furnace and melted in a graphite crucible. Once the aluminum was fully molten, the Al-25Si master alloy was gradually introduced and allowed to dissolve completely, ensuring uniform silicon distribution within the melt. Following this, the predetermined amount of Al-5Ti master alloy was added to incorporate titanium. The molten alloy was maintained at the target temperature and thoroughly stirred to promote homogeneity of all alloying elements. Degassing was subsequently performed using argon gas to eliminate dissolved hydrogen and entrapped oxides from the melt. The molten alloy was poured into preheated molds for solidification. The compositions of the alloys were determined by emission arc spectrometer (SPECTROMAXX LMX10) and the same has been reported in Table 1.

Table 1. Chemical composition of the as-cast alloys (wt.%)

Alloy	Elements (wt.%)							
	Si	Ti	Fe	Mn	Mg	Cu	Zn	Al
Al-15Si	15.00	ı	0.156	0.012	0.023	0.25	0.1	Bal

Al-15Si-0.5Ti	15.1	0.5	0.25	0.03	0.04	0.120	0.14	Bal
Al-15Si-1Ti	15.1	1.02	0.15	0.04	0.02	0.20	0.12	Bal
Al-15Si-2Ti	15.1	2.1	0.123	0.011	0.13	0.34	0.1	Bal

The spray atomization and deposition apparatus consist of a melting unit, an atomization assembly, a gas supply assembly, and a deposition substrate. The melting unit features a 5 kg capacity furnace with a maximum temperature of 1250°C (SILICARB Recrystallized (P) Ltd., India). The cast alloys were remelted to a superheated temperature in a furnace. The liquid melt stream disintegrates into micron-sized droplets at the bottom of the nozzle due to instabilities caused by the shearing effect of the high-velocity nitrogen gas jet. The semisolid atomized micron-sized droplets deposited onto the copper substrate. Figure 1 shows the photographic view and schematic diagram of spray atomization and deposition experimental setup. The process parameters of the alloys are shown in Table 2 as determined by pilot experiments. For example, a temperature between 100 - 150°C above the melting temperature of Al was used to ensure free flow of melt through the 4 mm nozzle during spray forming. A substrate distance of 390 – 395 mm provided good refinement in the microstructure of SF alloys. The SF equipment has been designed for a maximum pressure of 1 MPa. Therefore, a gas pressure range between 0.5 to 0.6 MPa was employed to provide a good atomization of melt into fine droplets. Finally, a flow rate range of 2.9 to 3 kg/min was used to avoid choking as well as clogging of the nozzle during spray forming. Table 3. shows the designations of the as-cast (AC) and spray-formed (SF) alloys for different compositions.



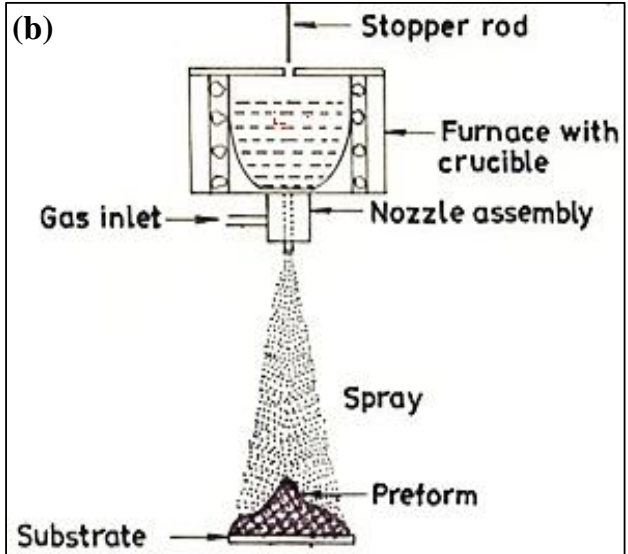


Figure 1. (a) The photographic view of experimental setup (b) schematic diagram of spray atomization and deposition process

Table 2. Process parameters employed in the present study

Alloy	Melt temperature	Substrate distance (mm)	Gas Pressure (MPa)	Melt flow rate (kg min ⁻¹)
Al-15Si	750	390	0.58	3.0
Al-15Si-0.5Ti	800	390	0.61	2.94
		670		
Al-15Si-1.0Ti	825	395	0.6	2.93
Al-15Si-2Ti	850	395	0.6	2.9

Table 3. Details of alloy designations

Alloy code	Alloy and Processing method
AC1	As-cast Al/15Si
AC2	As-cast Al/15Si/0.5Ti
AC3	As-cast Al/15Si/1Ti
AC4	As-cast Al/15Si/2Ti
SF1	Spray formed Al/15Si
SF2	Spray formed Al/15Si/0.5Ti
SF3	Spray formed Al/15Si/1Ti
SF4	Spray formed Al/15Si/2Ti

2.2. Microstructural investigation

For microstructure analysis, the samples were prepared from SF and AC alloys. Microstructural analysis of the AC and SF alloys was carried out using a light optical microscope (Lynx). The grain size and relative phase distribution were measured on optical micrographs using the linear intercept method following the procedure in ASTM E112-10 using Nascent Technology Inc. image analysis software. Scanning electron microscopy (SEM/EDS) (JEOL JSM-6480LV, 10–40 kV) was employed to study the microstructural features, and worn-out surfaces. Phase analysis of the SF and AC alloys was performed using an X-ray diffractometer (Rigaku Ultima) with CuK α radiation (λ = 0.15.404 nm), 30 kV and 40 mA and scanning at 2 θ = 10–80 degrees at a rate of 2 deg/min and energy dispersive X-ray spectroscopy (EDS).

2.3. Hardness and Wear characterization

The microhardness test was carried out using a Vickers microhardness tester at a load of 300 g and a dwell period of 15 seconds as per the E-384-ASTM standard. Five hardness tests were carried out on the polished surface at different points, and the average value of five readings was considered. A dry sliding wear test was carried out using a high-temperature tribometer (model: DUCOMTR-20LEDHM-PHM-800)in accordance with the ASTMG99-95standard. Cylindrical pins (8 mm

diameter, 30 mm length) were used for the room temperature test, and Figure 2 shows the pins (12 mm diameter, 20 mm shank portion) employed for the elevated temperature test. This modified pin features a blind hole for thermocouple insertion to measure the temperature near the sliding surface. The pin was heated using a heating element surrounding the shank portion, and the temperature was measured via a chromel–alumel thermocouple. Material loss was measured using a digital balance (Mettler AJ100). The contact surface was polished to 1200 grit and tested against a rotating EN-32 steel wear disc (HRC-65). The wear tests were repeated three times at a constant sliding speed of 1.0 m/s, sliding distance of 2000 m, and various normal loads (10, 20, 30, 40, and 50 N) at 30°C, 100°C, 200°C, and 250°C sliding temperatures. SEM analysis was conducted to examine the topography of the worn surfaces and wear debris formed during the test. Wear maps were developed based on the observations made on the wear modes and mechanisms.

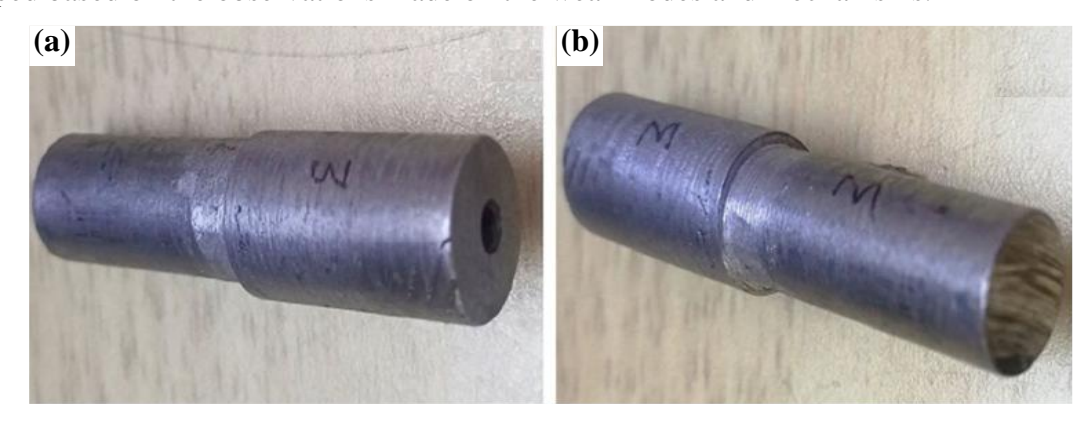


Figure 2. Photographs of wear test pin for elevated test conditions: (a) top end and (b) wear end

3. Results and Discussion

3.1. Phase analysis by XRD

The diffraction patterns of the AC alloys are shown in Figure 3. For each alloy, the diffraction patterns are similar. However, distinct alloys exhibit varying peak intensities. All the peaks were identified and consisted of only the Al, Si, and Al₃Ti phases. The X-ray diffraction data of the ACl alloy (Figure 3(a)) closely match the data provided in the JCPDS card (04--0787) at $2\theta = 38.473^{\circ}$ (111), 44.739° (200), and 65.135° (220). The peaks at $2\theta = 28^{\circ}$, 47°, 56° and 78° are attributed to crystalline Si with a cubic structure (JCPDS card No. 27--1402). The tetragonal phase of Al₃Ti (space group I4/mm) has lattice constants of a = b = 3.841 Å and c = 8.585 Å, which are consistent with the values in the standard cards (JCPDS No. 65--0429). The Al₃Ti peaks shown in Figure 3(b), (c) and (d) were associated with the AC2 and AC3 and AC4 alloys, respectively. As the Ti content in the alloy increased, the intensity of the Al₃Ti peak decreased.

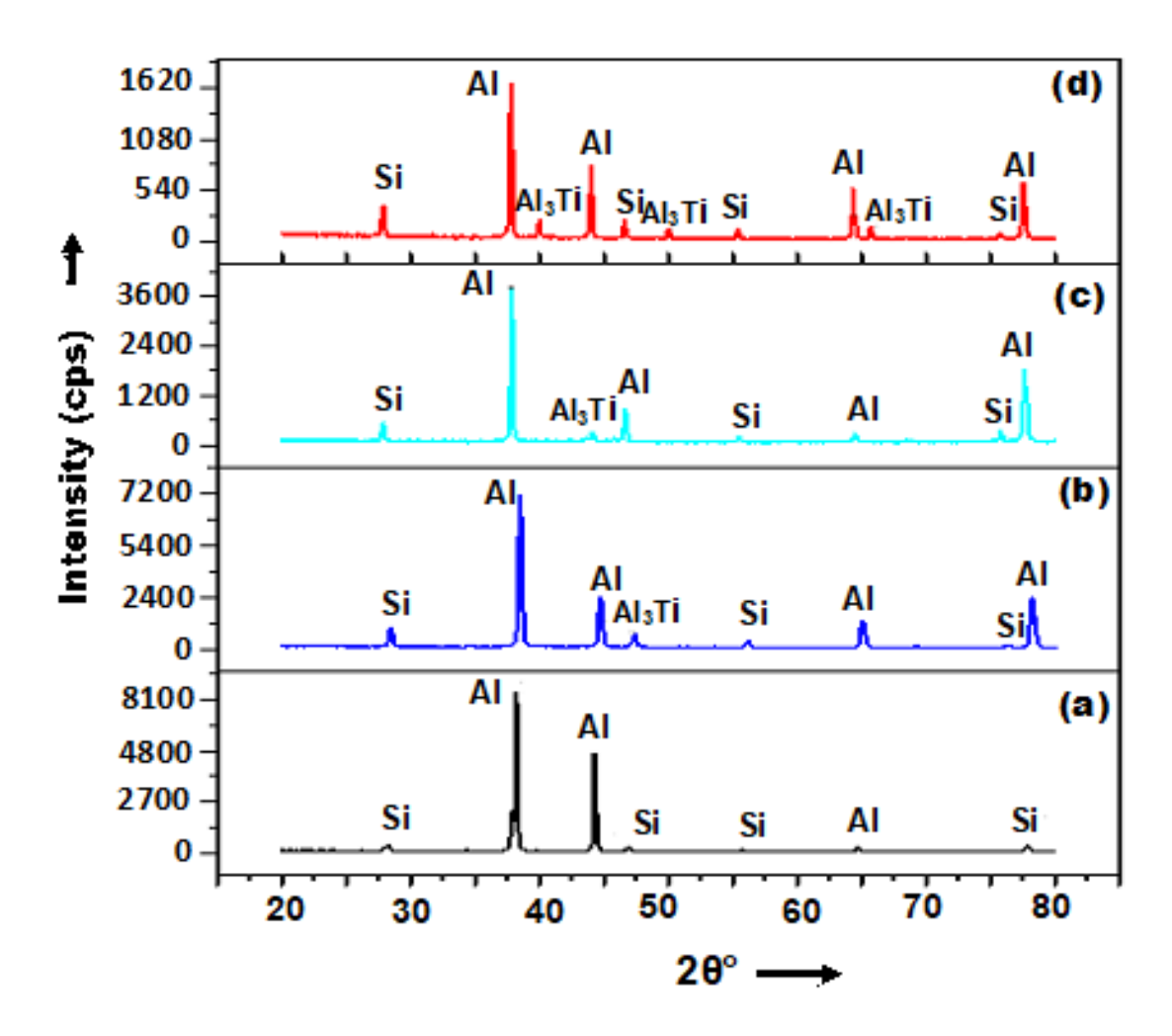


Figure 3. XRD patterns of (a) AC1, (b) AC2, (c) AC3, and (d) AC4 alloys

The representative XRD patterns of the SF1, SF2, SF3 and SF4 alloys are shown in Figure 4. The peak intensities of the Al phase are greater for the SF alloys than for that of the AC alloys. The Al phase average lattice parameters (from the ICDD) of the SF1 and AC1 alloys are 4.047 Å and 4.052 Å, respectively. For the SF4 and AC4 alloys, the average lattice parameters are 4.0436 Å and 4.0506 Å, respectively. The lattice parameter of Al for SF alloys is lower than that for the AC alloys.

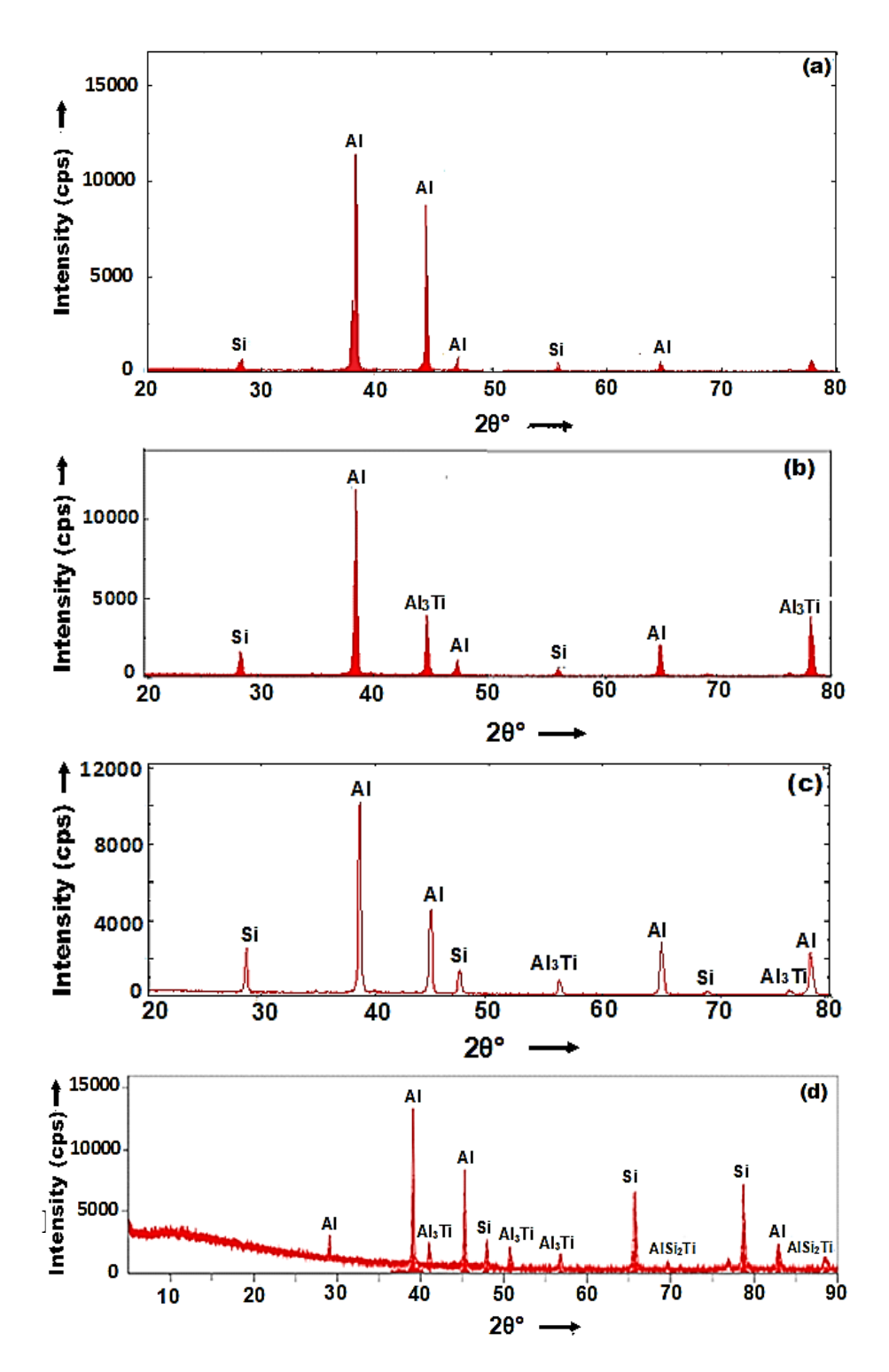


Figure 4. XRD patterns of the (a) SF1, (b) SF2, (c) SF3 and (d) SF4 alloys

3.2 Microstructural features

Figure 5 displays the optical microstructures of the AC alloys, revealing significant variations in their microstructural features. The AC1 alloy exhibited large primary Si crystals (30–90 μ m), needle-like eutectic Si (30–150 μ m), and a dendritic α -Al matrix. The microstructure of the AC2 alloy is similar, with additional flake-like intermetallics. As the Ti content increases, distinct microstructural changes emerge. The AC3 alloy features block-like primary Si, needle-like eutectic Si, and petal-like Ti-rich intermetallic particles. The AC4 alloy consists of large primary Si particles

and a dendritic Al matrix with randomly distributed Ti-rich intermetallics. Notably, increasing the Ti content promoted the formation of diverse Ti-rich intermetallic phases, significantly influencing the microstructures of the alloys.

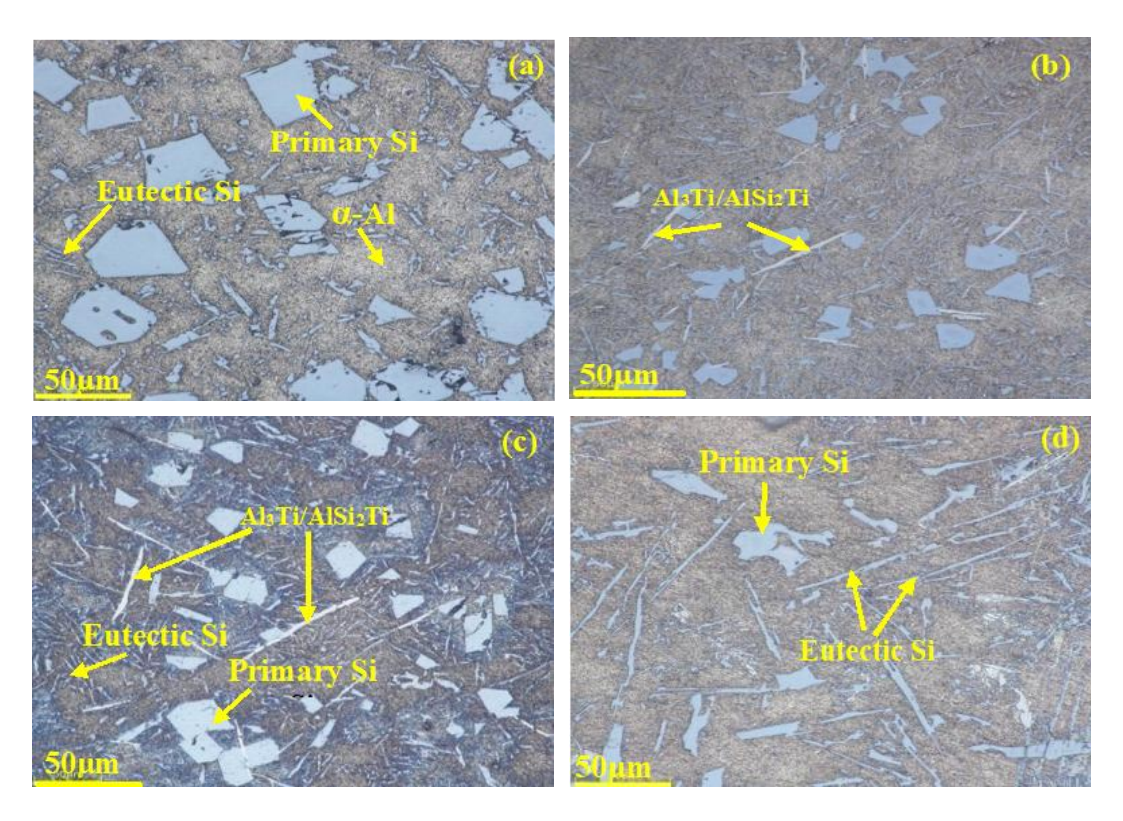


Figure 5. Optical microstructures of (a) AC1, (b) AC2, (c) AC3, and (d) AC4 alloys

Table 4 presents the grain diameter and grain area measurements of the AC1 alloy obtained by the intercept method.

Table 4: Details of grain analysis of AC alloys

Allow	Grain size	(µm)	Average	Avg. Grain
Alloy	Min	Max	Diameter (µm)	Area (mm²)
AC1	8.15	228.0	154.00	0.046
AC2	11.2	508	138.79	0.042
AC3	9.4	359	129.85	0.041
AC4	11.0	302	171.35	0.065

Correspondingly, Figure 6 shows the image analysis results of the AC alloys and the automated quantification of their microstructures. The results of the particle sizes of the different phases in the AC alloys are presented in Table 6. The primary Si $(20-150~\mu m)$ and eutectic Si $(20-200~\mu m)$ particle sizes decrease with increasing Ti content, whereas the average grain size increases from $11.2-15.3~\mu m$. The results indicate that increasing the Ti content in the Al-15Si alloys refined the microstructure, reducing the primary Si and eutectic phase sizes while increasing the Al₃Ti and AlSiTi particles and increasing the Ti-rich intermetallic phase area. The phase distributions of AC1

and AC2 differ significantly. AC1 consists of α -Al (57%), Si (19%), and eutectic (23%) phases, whereas AC2 comprises α -Al (35%), Si (19%), eutectic (20%), and Al₃Ti intermetallic (19%) phases. Microstructural analysis revealed Al₃Ti flakes of various sizes in the matrix and coarsening of the α -Al, primary Si, and eutectic Si phases.

The morphology of the Ti-rich intermetallic phases depends on the solidification conditions. Flakes form under slow solidification, whereas petal-like shapes develop with large thermal gradients due to rapid cooling. Conversely, low-temperature solidification with high Ti saturation yields faceted blocky aluminide, characterized by cubic to long flat plate shapes [13]. The results of quantitative image analysis and the particle sizes of the different phases in the AC alloys are listed in Table 4 and Table 5. The results indicate that the area of both the primary and eutectic Si phases decreases with increasing Ti content from 0.5 wt.% to 2.0 wt.%, resulting in an increase in the Ti-rich intermetallic (Al₃Ti and AlSi₂Ti) phase area from 12.8% to 32.8%.

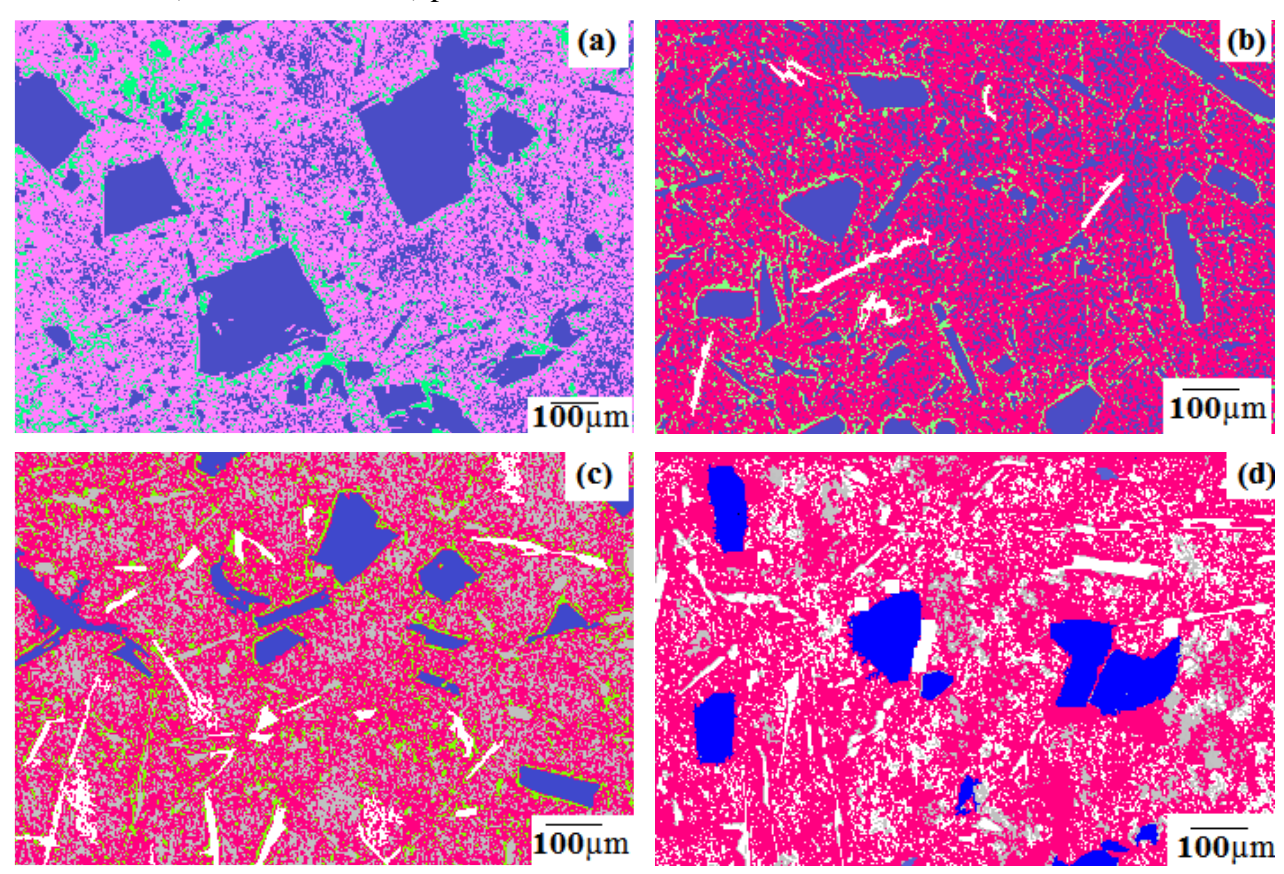


Figure 6. Optical micrographs and phase analysis of (a) AC1, (b) AC2, (c) AC3, and (d) AC4 alloys

Table 5. Automated quantification of microstructure of AC cast alloys. (Colors are associated with corresponding micrographs presented in Figure 6)

	AC1 alloy			AC2 alloy			
Color	Phase	Area (%)	Color	Phase	Area (%)		
Color	Si	10.44		Primary Si	9.06		
	α-Al	55.51		α-Al	48.6		
	Eutectic Si	36.46		Eutectic Si	26.46		
	(a)			Ti Intermetallic	12.80		
	AC3 alloy			AC4 alloy			
Color	Phase	Area (%)	Color	Phase	Area (%)		
	Primary Si	8.73		Primary Si	8.23		
	α-Al	42.26		α-Al	38.26		
	Eutectic Si	23.46		Eutectic Si	17.4		
	Ti intermetallic	22.80		Ti intermetallic	32.80		

Table 6. Results of particle sizes (µm) of different phases in the AC alloys

Alloy	Primary Si		Euteo	ctic Si	Al ₃ Ti/AlSi ₂ Ti	
Alloy	Min	Max	Min	Max	Min	Max
AC1	20	150	20	200	-	-
AC2	18	114	17	154	20	150
AC3	15	90	15	113	28	164
AC4	12	87	13	98	30	194.8

Figure 7 presents the SEM micrograph of the AC1 alloy. The microstructure consists of coarse primary Si particles (50–150 μ m) with polygonal irregular crystals interspersed with needle-like eutectic Si that are unevenly distributed in the α -Al matrix. The EDS analysis results of the AC1 alloy are shown in Figure 8, revealing three distinct phases in the microstructure: eutectic Si (Field 1), primary Si (Field 2), and the α -Al matrix (Field 3). The primary Si phase appears light gray, exhibiting a block-like or plate-like morphology, whereas the eutectic Si phase appears dark gray, displaying a needle-like structure.

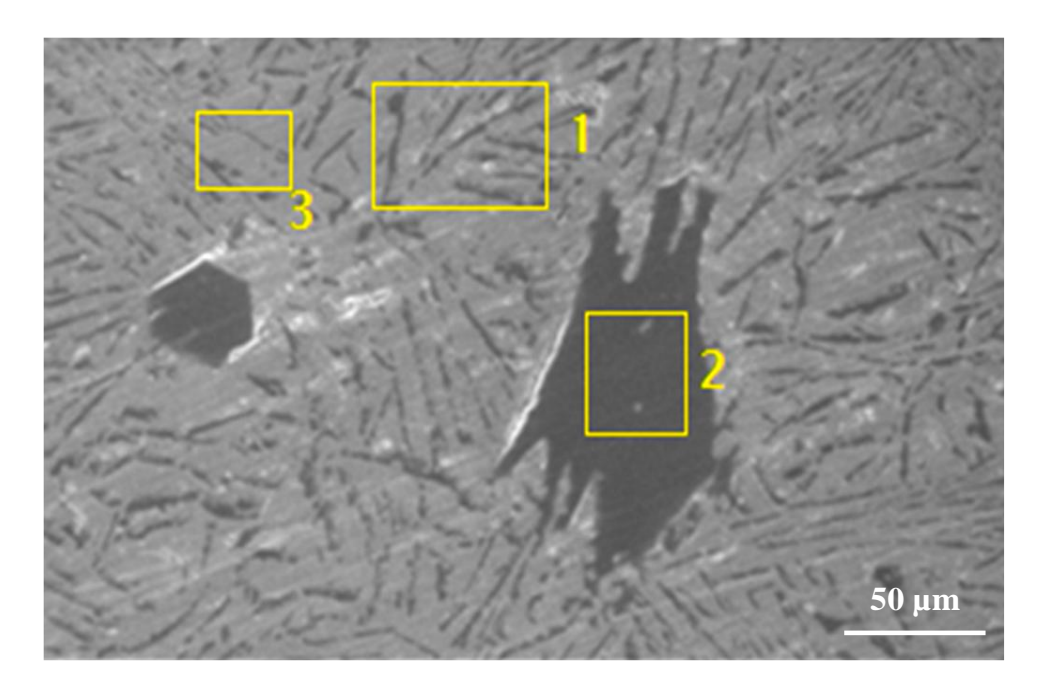


Figure 7. SEM/EDS micrograph of the AC1 alloy

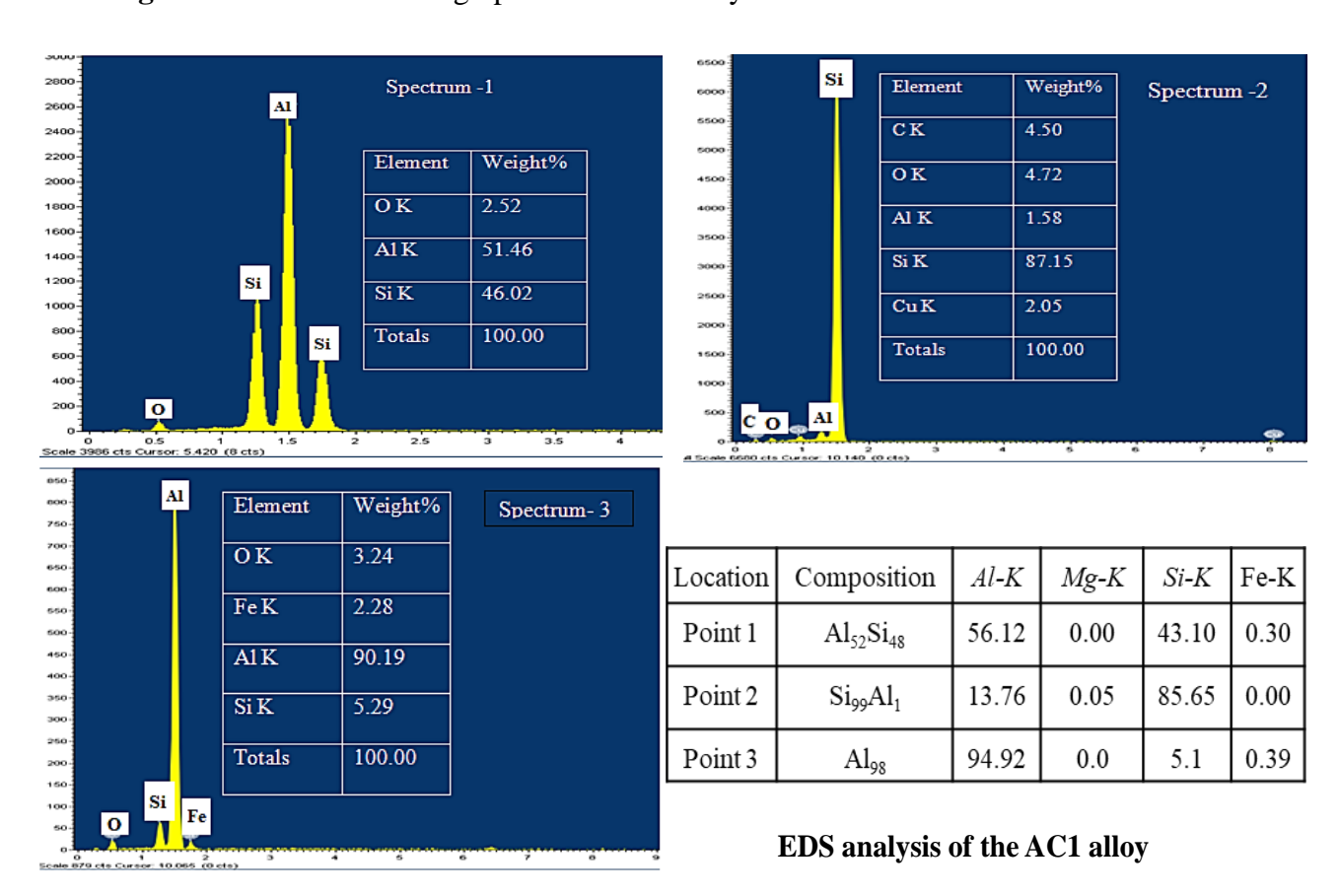


Figure 8. EDS spectrum and phase composition of the AC1 alloy

Figure 9 shows the SEM microstructure of the AC2 alloy, which consists of coarse primary Si, needle-like eutectic Si, and Al-Si-Ti intermetallic phases dispersed in the α -Al matrix.

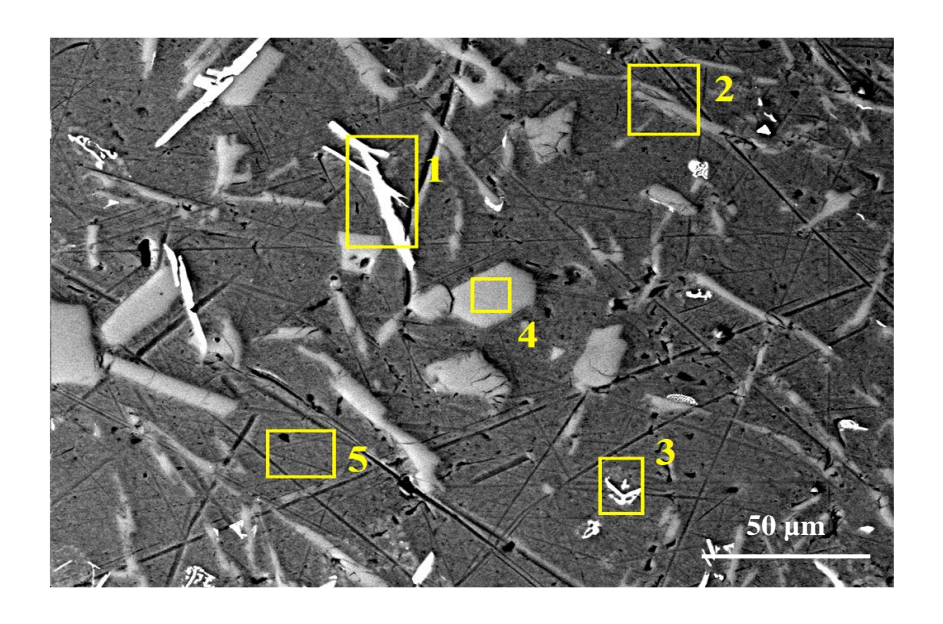


Figure 9. SEM/EDS microstructure of the AC2 alloy

EDS analyses (Figure 10) of the AC2 alloy confirmed the presence of these phases, with the Al-Si-Ti intermetallics exhibiting flake-like or petal-like morphologies.

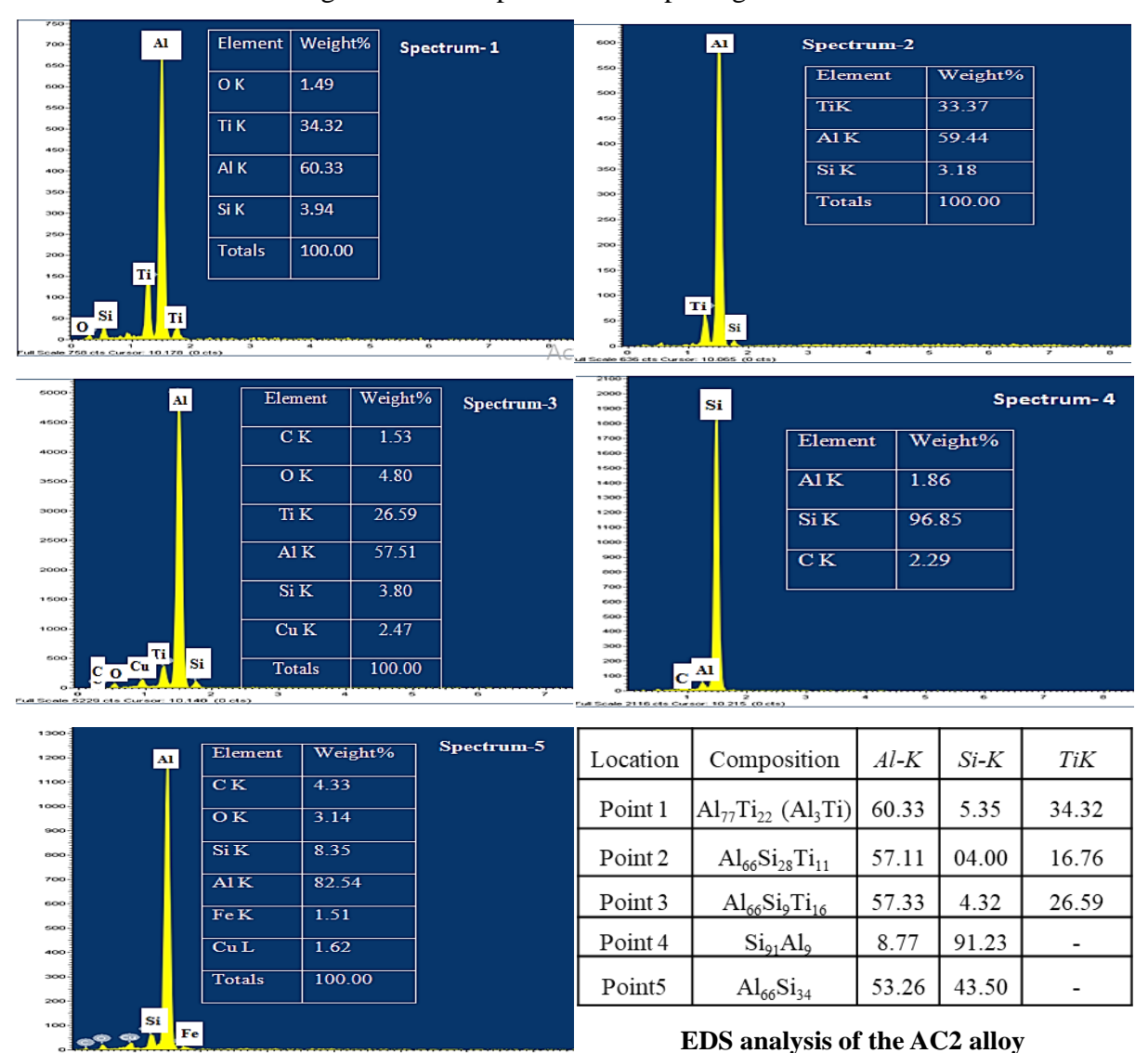


Figure 10. EDS spectrum and EDS analysis of the AC2 alloy

In contrast, the SEM microstructure of the AC3 alloy (Figure 11) shows a greater volume proportion of Ti-rich intermetallic phases together with primary Si and eutectic Si in the α -Al matrix. The EDS spectrum (Figure 12) verified the composition of these phases, revealing sharp needle-like and flake-like Ti intermetallic particles.

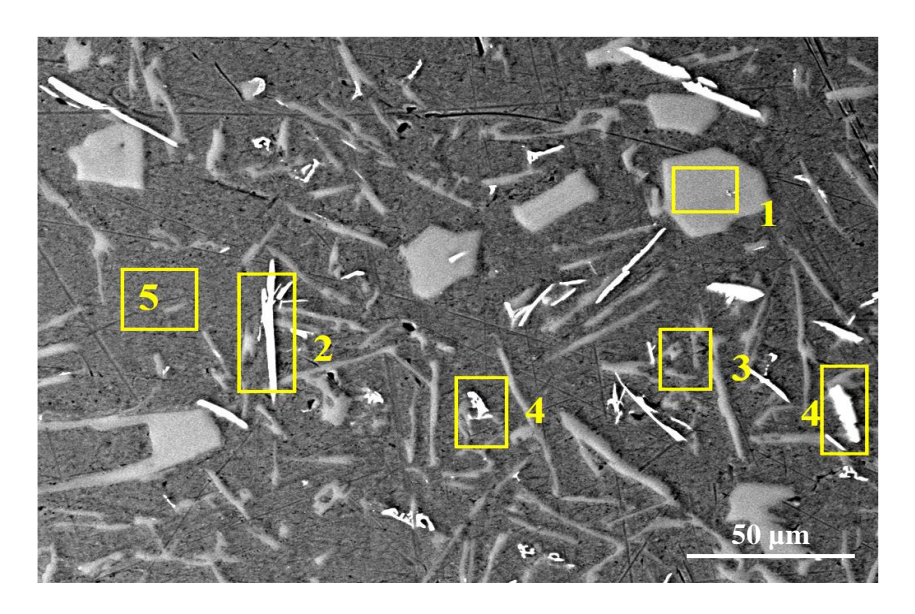


Figure 11. SEM/EDS micrograph of the AC3 alloy with EDS points

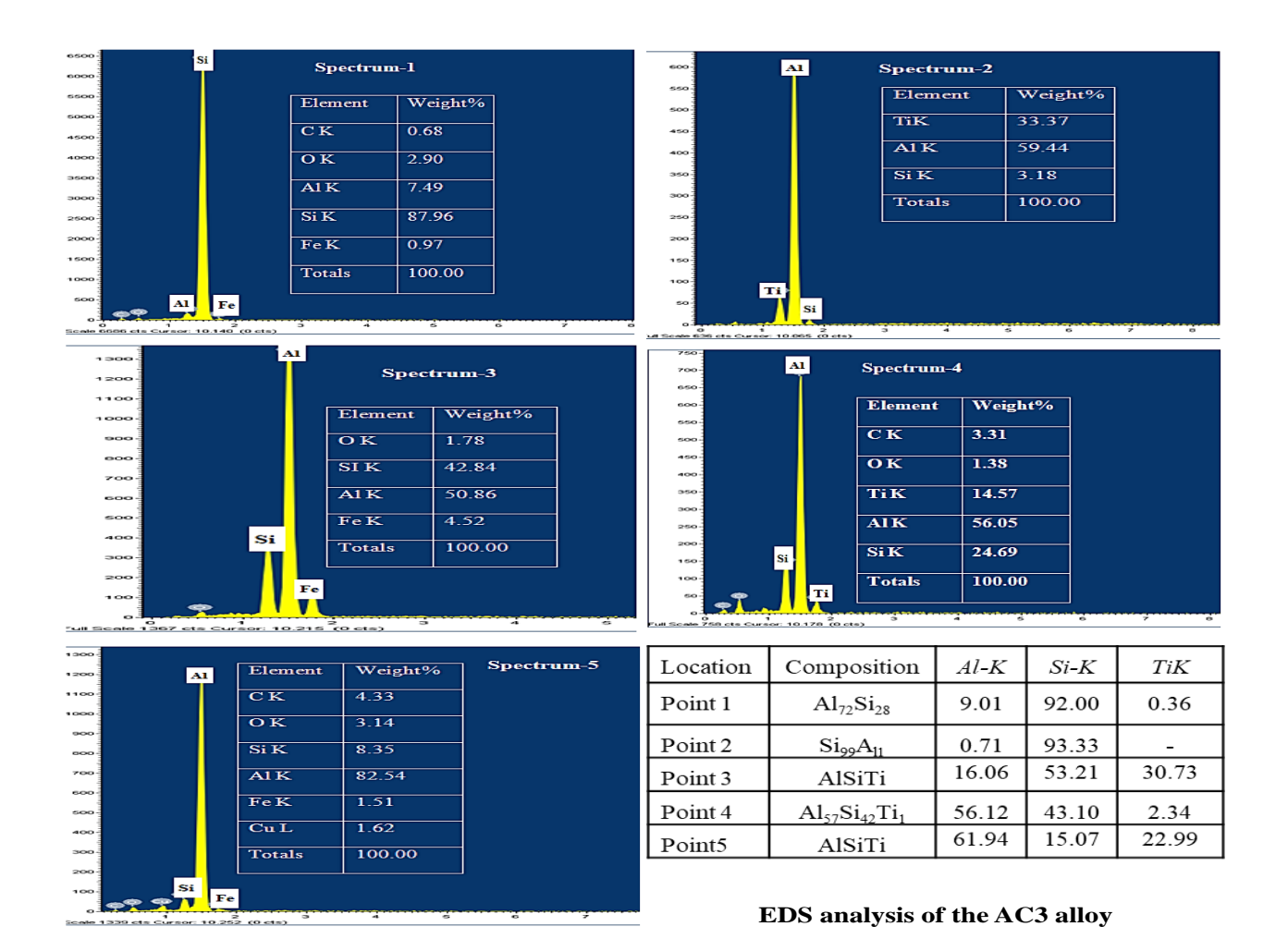


Figure 12. EDS spectrum and EDS analysis of the AC3 alloy

Figure 13 shows the AC4 alloy microstructure, featuring large primary Si crystals, slender eutectic Si needles, and abundant Ti-rich intermetallic phases (flakes and needles) in the α -Al matrix (confirmed by EDS analysis, Figure 14). Notably, α -Al and eutectic Si coarsening exceeds that of the base alloy.

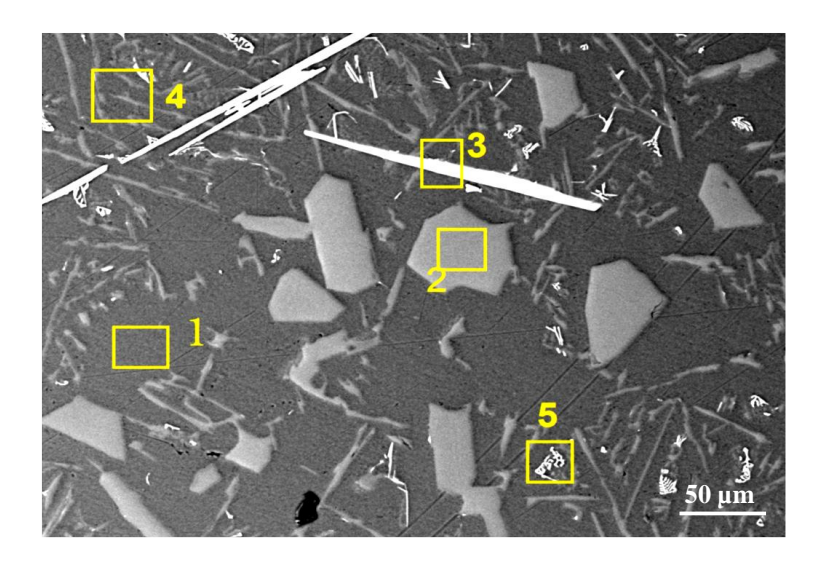


Figure 13. SEM/EDS microstructure of AC4 alloy

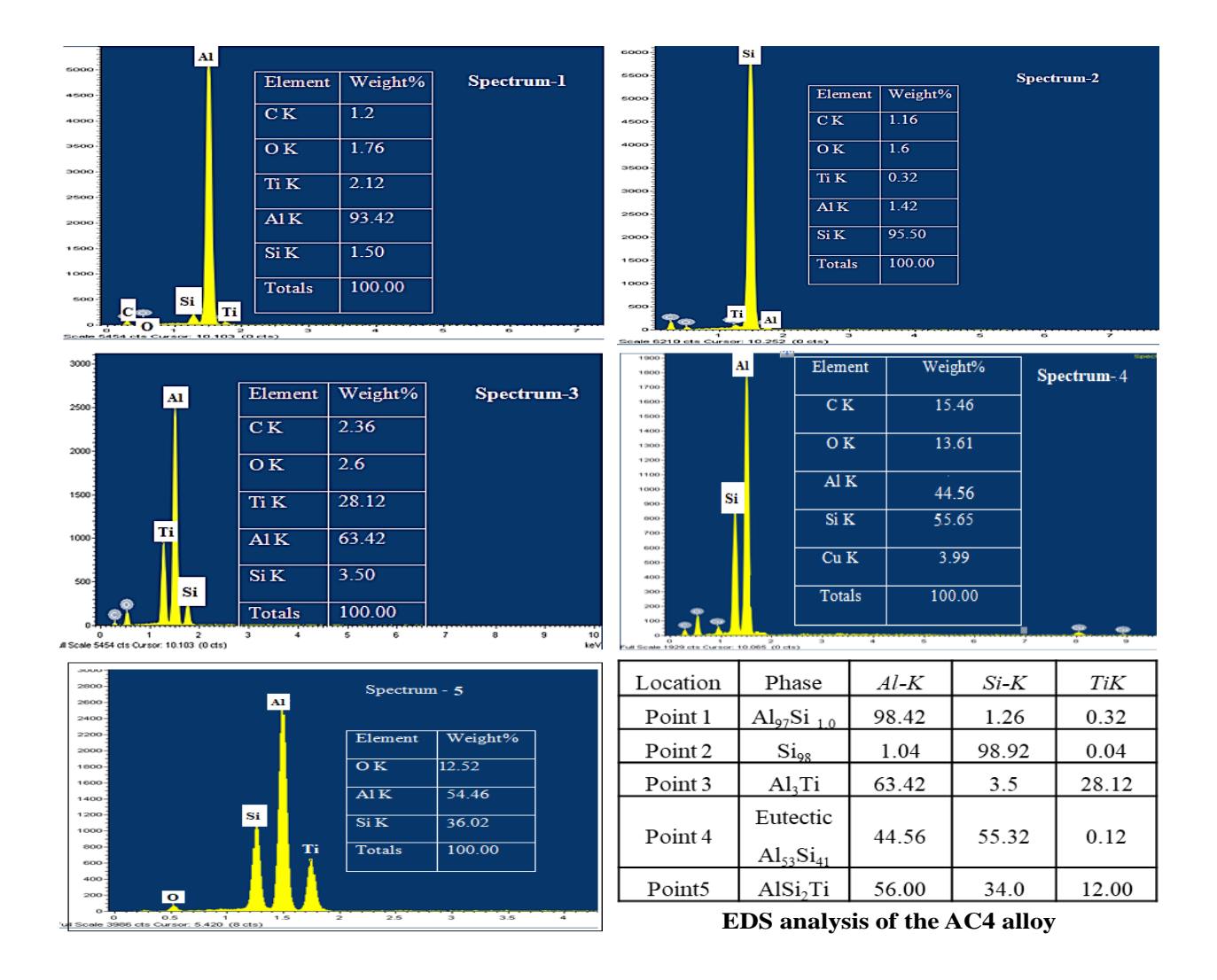


Figure 14. EDS spectrum and EDS analysis of the AC4 alloy

Figure 15 shows the optical microstructures of the SF alloys. SF1 exhibited uniform globular primary and eutectic Si particles (5-10 μ m) in equiaxed Al. SF2 featured fine Ti intermetallic plates (10-15 μ m), primary/eutectic Si (3-10 μ m), and equiaxed Al grains. SF3 displays fine Si (2-15 μ m), isolated eutectic Si, and Ti-rich intermetallics (15-20 μ m). SF4 has a finer primary Si phase, blunted eutectic structure, and spherical Ti intermetallics (15-25 μ m). Microstructural analysis revealed an increased Ti intermetallic phase volume fraction across the alloys.

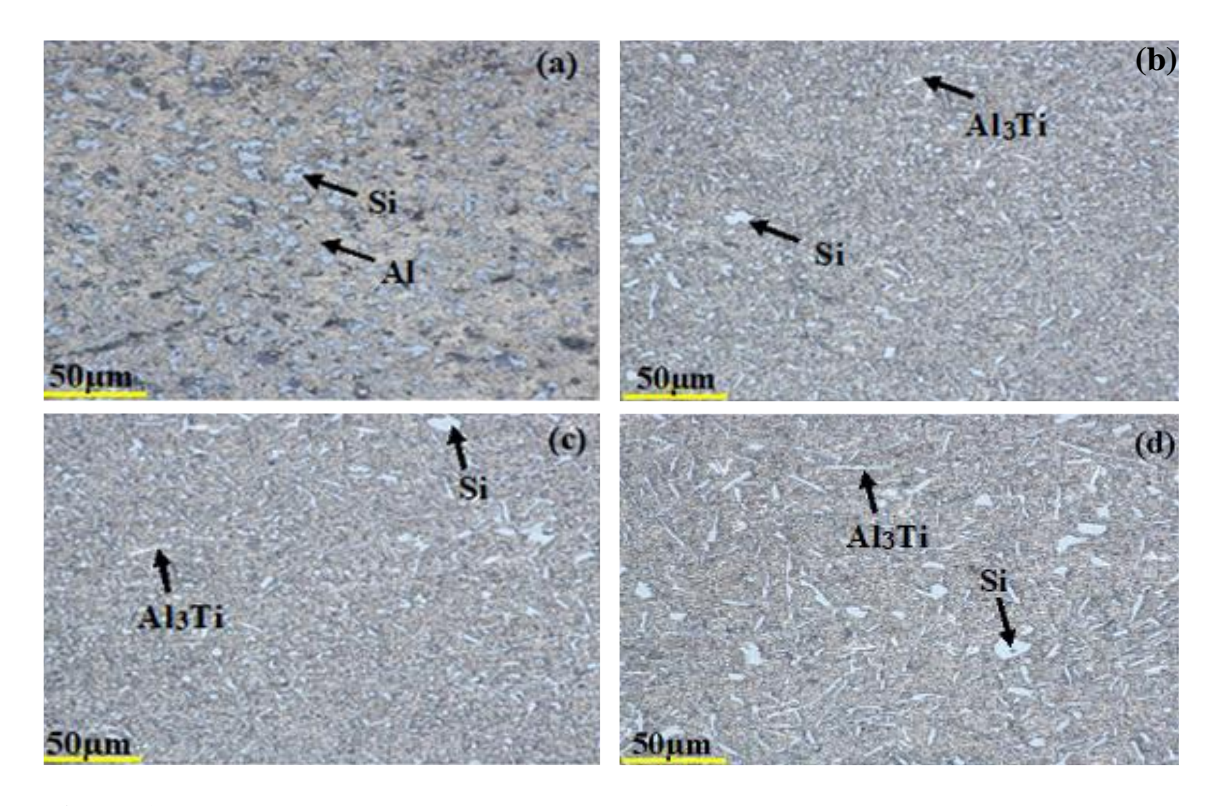


Figure 15. Optical micrographs of SF alloys (a) SF1 (b) SF2 (c) SF3 and (d) SF4

Table 7 presents the image analysis results of the SF alloys obtained via the intercept method, highlighting their microstructural characteristics. The SF1 alloy has a mean grain diameter of 13 μ m, with a phase distribution consisting of α -Al (56%), Si (25%), and eutectic phases (13%). Notably, the introduction of Ti into SF2-SF4 alloys leads to substantial grain growth, with average grain sizes ranging from 14 μ m to 24 μ m, increasing with increasing Ti content.

Table 7. Details of grain analysis of SF alloys

Allow	Grain s	ize (µm)	Average	Avg. Grain Area
Alloy	Min	Max	Diameter (µm)	(\mathbf{mm}^2)
SF1	3.3	28.0	13.0	0.00023
SF2	3.6	37 .8	13.76	0.00027
SF3	4.0	45.23	14.00	0.00028
SF4	6.7	63.5	24.17	0.00045

Table 8 presents the details of the microstructural image analysis of the SF alloys, revealing significant changes in the phase distribution with increasing Ti content. The Si phase area decreases marginally from 40% to 34%, whereas the α-Al phase area decreases substantially from 56% to 36.5%. Conversely, the Ti-rich intermetallic phase area increases remarkably from 12.8% to 30%, dominating the microstructure. The SF4 alloy exhibited a balanced phase distribution of 36% Al, 34% Si, and 30% Ti-rich intermetallic phases, with no eutectic phases present. Notably, rapid solidification through spray forming yields significantly finer grains in SF alloys than in AC alloys,

producing homogeneous and nearly spherical Si and intermetallic particles within the equiaxed Al matrix.

Table 8. Results of the particle size (μ m) of the different phases in the SF alloys

Allow	Si (µm)		Eutectic Si (µm)		Ti intermetallic (μm)		
Alloy	Min	Max	Min	Max	Min	Max	
SF1	5	10	7	12	4.5	26.6	
SF2	7	15	10	15	3.3	28.8	
SF3	3	22	9	17	4.0	32.3	
SF4	5	27	6	19	6.7	36.5	

Figure 16 shows the SEM/EDS microstructures of the SF1-SF4 alloys, revealing a homogeneous distribution of fine primary and eutectic Si particles within the equiaxed Al matrix. The SF1 alloy (Figure 16(a)) exhibited uniform primary Si and eutectic Si particles, with EDS analysis indicating enhanced solid solubility of Si (13.8 wt.%) in the α-Al matrix (86.1 wt.%) due to rapid cooling during spray formation. The SF2-SF4 alloys (Figure 16 (b-d)) displayed fine globular primary and eutectic Si particles, accompanied by short rod-like Al-Si-Ti intermetallic phases within the equiaxed α-Al matrix. EDS analysis revealed the presence of AlSi₅Ti₃, a short gray rod-like intermetallic phase, alongside white primary Si and eutectic Si phases. The composition of the AlSi₅Ti₃ intermetallic phase aligns with previously reported values by Gupta [22], confirming its presence in the alloy. During semi-solidification, reduced surface energy leads to lower aspect ratios, causing Si particles to transform into spherical or equiaxed shapes. This microstructural evolution underscores the effectiveness of spray forming in producing refined, homogeneous microstructures with improved solid solubility, which differ significantly from those of cast alloys As-cast hypereutectic Al-Si alloys typically exhibit coarse primary Si particles (blocks, fish bones, hoppers, stars, plates) and eutectic Si in acicular, flake-like, or fibrous forms. Primary Si crystals form through nucleation and growth, with the size and volume fraction inversely proportional to the solidification rate. Research has explored the microstructural characteristics of spray-formed hypereutectic Al-Si alloys [23, 24]. The SF2 alloy exhibited a uniform distribution of Si and intermetallic particles due to rapid cooling of the atomized droplets, preventing primary Si and intermetallic phase growth. This yields refined microstructures with fine, evenly dispersed primary Si, eutectic Si, and Ti-rich intermetallic particles. Rapid solidification (10³–10⁶ K/s) in SF alloys produces equiaxed Al grains and particulate Si structures shaped by fracture and impact deformation during atomization and deposition [25,26]. Spray forming uniquely alters the stability of Si- and Ti-rich phases, yielding refined microstructures with distinct properties. During deposit build-up, prolonged fragmentation and coarsening of partially solidified droplets significantly alter Si phase morphological stability due to high cooling rates and recurrent deformation. As solid, semisolid, and liquid droplets impact the surface, numerous fragments form, serving as

heterogeneous nucleation sites. These nuclei or existing fragments then grow or coarsen in the solidifying layer due to intense agitation and cooling, forming equiaxed structures. Notably, primary Si particles in the top layer suppress eutectic Al–Si formation, enhancing Si nucleation [27, 28]. Differentiating Si particles formed through various mechanisms is challenging, leading to modified primary and eutectic Si morphologies in spray-deposited alloys and significantly refined grain sizes. The high-velocity impact of semisolid/liquid droplets on the substrate fragments dendrites and solid phases generates additional nucleation sites from debris and yields a refined microstructure [29].

The addition of titanium to Al-Si alloys refines the grain size, but excess Ti can cause liquid metal process issues and casting defects due to coarse Al-Si-Ti particle precipitation [30]. Despite this, research on Al-Si-Ti intermetallic phases in Al-Si-Ti alloys remains limited, unlike the well-studied Al-Ti intermetallics in binary Al-Ti systems, which facilitate grain refinement [31]. The Al-Si-Ti alloy system underwent complex phase transformation, with various ternary intermetallic phases forming in the aluminum-rich region. However, identifying these phases is challenging because of their diverse compositions and lattice characteristics. Spray-deposited hypereutectic Al-Si-Ti alloys deviate from equilibrium solidification, involving metastable phase crystallization, primary Si nucleation and growth on Al₃Ti, and asymmetric ternary eutectic formation (α -Al, Si, Al₃Ti, and Al-Si-Ti). The high metastable phase content arises from a strong tendency for metastable phase formation and sluggish metastable-to-equilibrium phase transition kinetics. Solidification occurs in two stages: rapid cooling during gas atomization, where Al₃Ti forms within droplets, followed by slow cooling during droplet consolidation, allowing transformation to the stable Al-Si-Ti phase upon deposition.

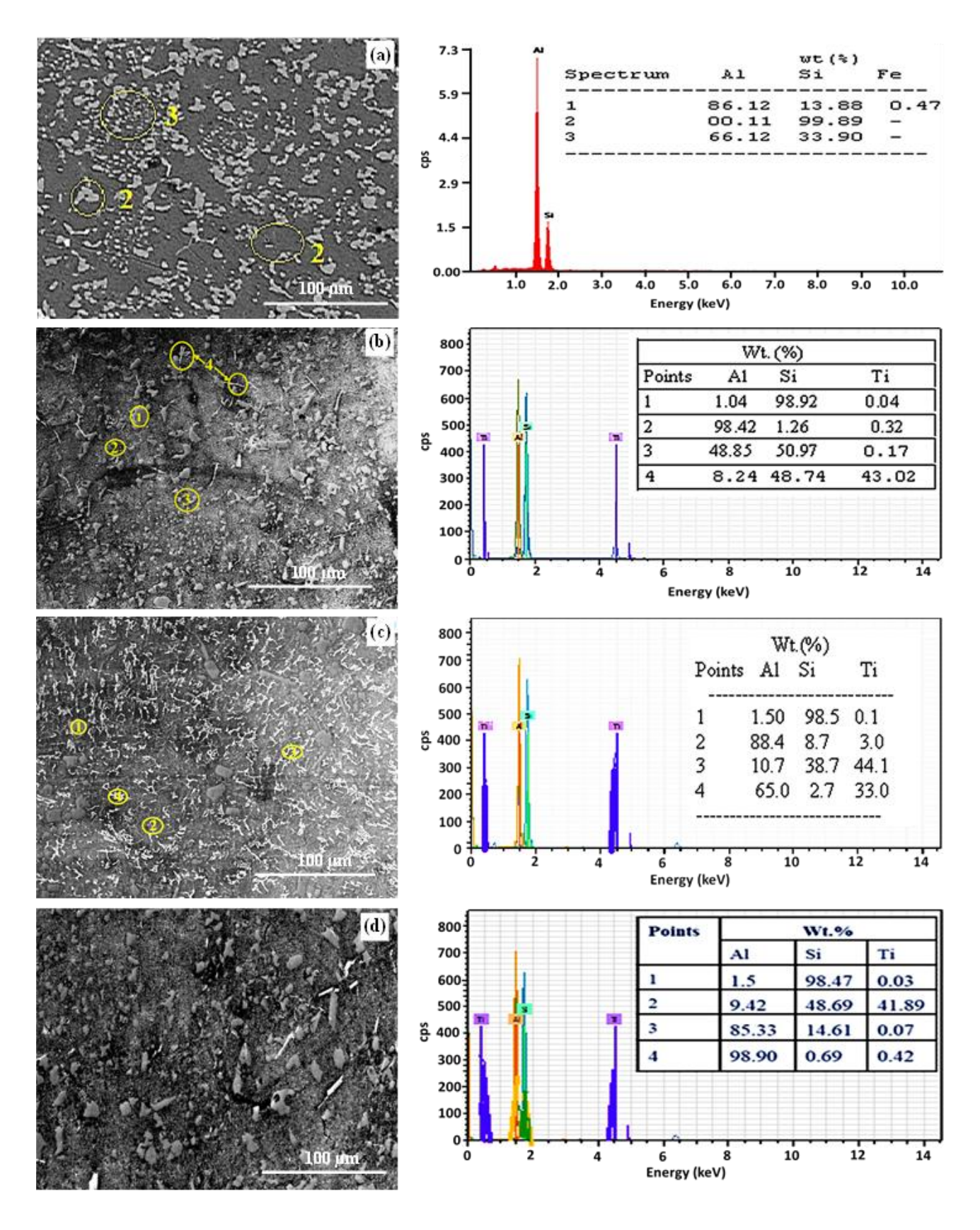


Figure 16. SEM/EDS microstructures of the SF alloys (a) SF1, (b) SF2, (c) SF3, and (d) SF4

3.3. Hardness

Figure 17 shows the Vickers hardness values of the AC and SF alloys at various temperatures. Notably (Figure 17(a)), the hardness of the Ti-containing alloys (AC2-AC4) was consistently greater than that of the base alloy (AC1) across all the temperatures (25°C to 250°C). The addition of Ti substantially increased the hardness, mitigating the decrease with increasing temperature. The AC4 alloy had the highest hardness at all temperatures, with values 41–52% greater than those of AC1 and 15–20% greater than those of AC2 and AC3. This suggests a significant hardening effect of Ti addition, particularly in the AC4 alloy. Figure 17(b) reveals that the SF alloys had a greater microhardness than did the AC alloys across all the temperatures, with the hardness increasing with increasing Ti content because of the presence of Ti-rich intermetallic phases. Although the hardness decreased with temperature, the SF alloys retained higher values.

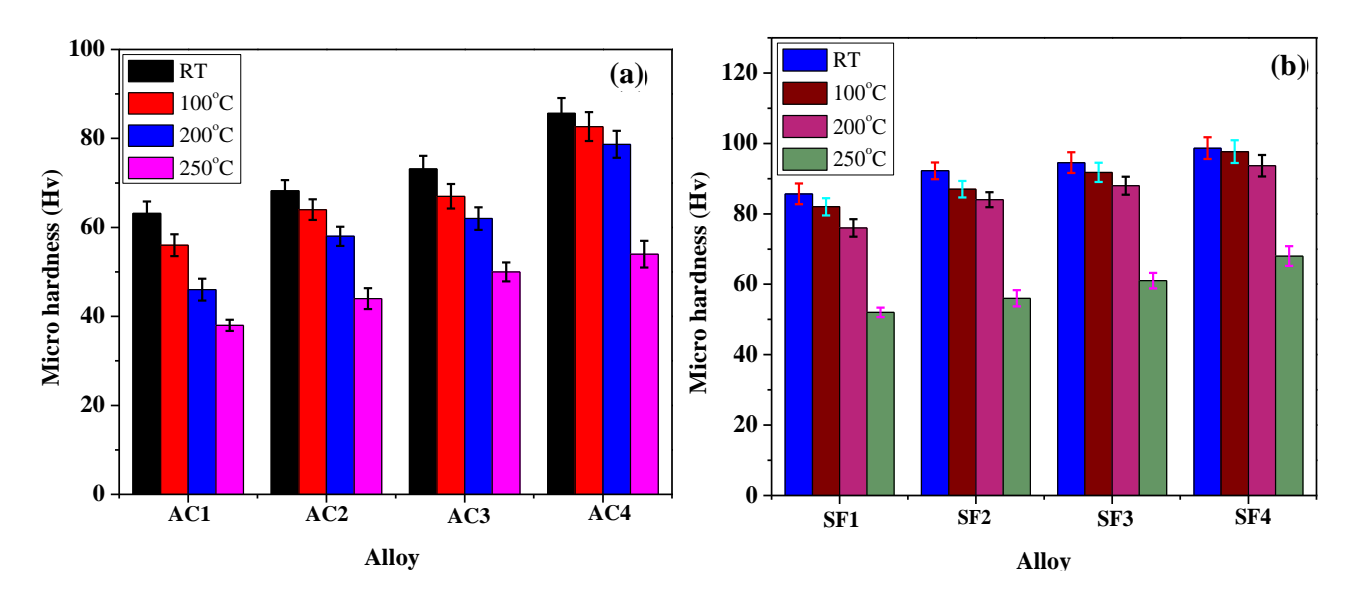


Figure 17. Variation in hardness with temperature of (a) AC and (b) SF alloys

Table 9 and Table 10 show the percentage decrease in hardness of the SF and AC alloys with temperature. AC1 experiences the greatest hardness reduction (39.80%) at 250°C, making it the most affected by temperature, whereas AC4 retains the greatest hardness at 100°C, with only a 3.5% loss, indicating better thermal stability. AC2 and AC3 show moderate hardness reductions with increasing temperatures, but AC3 maintains better hardness overall than does AC2. All the AC alloys experienced significant losses at 250°C, with AC1 being the most affected and AC4 showing the best retention. Among the SF alloys, SF4 has the least hardness reduction at all temperatures, making it the most thermally stable. SF1 and SF2 show a significant decrease of approximately 39% at 250°C, indicating greater sensitivity to temperature, whereas SF3 performs better than SF1 and SF2 in terms of hardness retention at high temperatures. All the SF alloys exhibit a relatively small hardness decrease up to 200°C but experience a sharp drop at 250°C. Table 10 shows the percentage of increase in the hardness of the SF alloys over that of the AC alloys at different temperatures. In terms of hardness improvement, SF1 has the greatest increase (65.22%) at 200°C

compared with that of AC1. SF2 and SF3 alloys follow similar trends, with hardness increasing by approximately 30–45% across all temperatures. SF4 has the lowest improvement at lower temperatures (15.19% at 25°C) but performs better at higher temperatures, with a 25.93% increase at 250°C. Overall, compared with AC alloys, SF alloys demonstrate greater hardness retention at elevated temperatures.

Table 9. Hardness reduction in % from 25°C to 100°C, 200°C, and 250°C for each AC and SF alloys.

Alloy	25°C to 100°C	25°C to 200°C	25°C to 250°C
AC1	11.34	27.15	39.80
AC2	6.20	15.00	35.50
AC33	8.38	15.20	31.63
AC4	3.50	8.17	36.97
SF1	4.28%	11.29%	39.30%
SF2	5.67%	8.92%	39.28%
SF3	2.92%	6.92%	35.48%
SF4	1.01%	5.07%	31.08%

Table 10. The percentage increase in hardness of SF alloys over that of AC alloys at different temperatures

Alloy comparison	25°C	100°C	200°C	250°C
SF1 vs AC1	35.64%	46.43%	65.22%	36.84%
SF2vsAC2	35.18%	35.94	44.83	27.27
SF3vsAC3	29.29%	36.99%	41.94%	22.00%
SF4 vs AC4	15.19%	18.16%	19.08%	25.93%

Figure 18 compares the hardness of the AC and SF alloys across all the temperatures, revealing that the SF alloys consistently outperform the AC alloys. This increased hardness stems from the increased hard Si volume fraction, homogeneous distribution of fine Si and intermetallic phases, and solid solution strengthening due to rapid solidification. These combined effects make SF alloys suitable for high-performance applications [32,33]

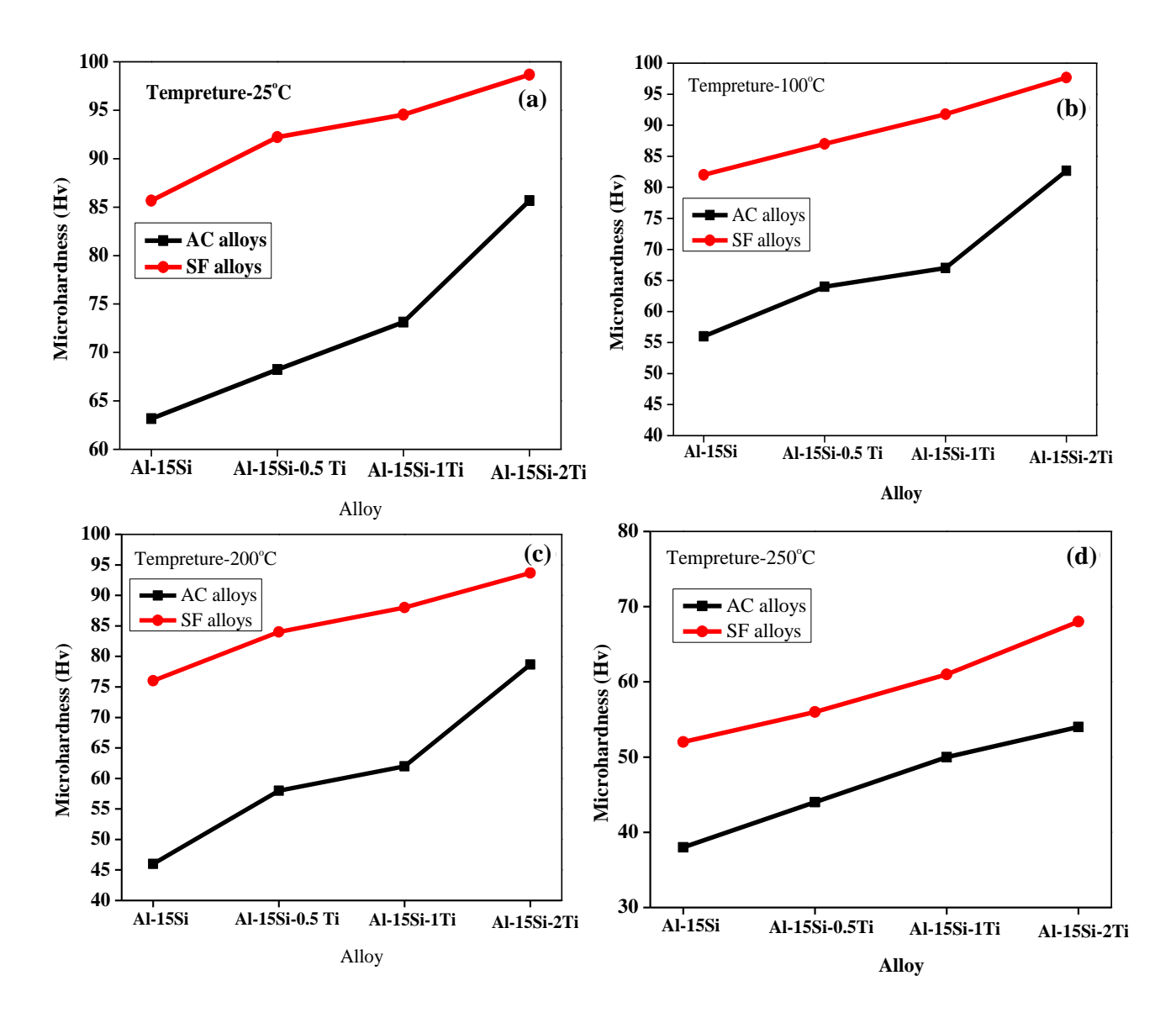


Figure 18. Variation in hardness of AC and SF alloys at (a) 25°C, (b) 100°C, (c) 200°C, and (d) 250°C

The Hall–Petch equation describes the relationship between the grain size and hardness, as given by Equation (1)[34].

$$H_{\nu} = H_{\nu_0} + k \frac{H_{\nu}}{\sqrt{d}} \tag{1}$$

where H_v denotes the hardness of the polycrystalline metal, 'd' signifies the grain size, and H_{v_0} and kH_v are constants.

The equation shows that as the grain size decreases, the hardness increases, indicating that smaller grains lead to stronger, more resistant materials. The superior hardness of the SF alloys at both room and elevated temperatures could be due to the fine and uniformly distributed hard Si phases that resist plastic deformation during indentation and the thermally stable Al₃Ti and AlSi₂Ti phases in the equiaxed Al matrix that provide localized strength.

The temperature dependence of hardness in polycrystalline materials is often described by equation (2)[35].

$$H_{v} = A e^{-BT} \tag{2}$$

where H_{ν} is the hardness, 'T' is the test temperature (in Kelvin), and A and B are constants.

This equation shows that the hardness decreases linearly with increasing temperature, with the rate of decrease determined by coefficient 'B'. This study revealed that the hardness of AC and SF alloys consistently decreases with increasing temperature, which is driven by thermal activation. Thermal activation causes atomic vibrations, softening and expanding of the microstructure, which significantly influences hardness. The hardness of the AC1 alloy decreases sharply due to softening of the eutectic Si and α-Al phases, reducing its resistance to plastic deformation. In contrast, in AC2-AC4 alloys, Ti forms thermally stable intermetallics (Al₃Ti and AlSi₂Ti), enhancing resistance to plastic deformation and preserving hardness at elevated temperatures.

3.4. Tribological characteristics

3.4.1. Volumetric wear rate

Figure 19 (a) shows the load-dependent wear rates of the AC alloys at 25°C and 1.0 m/s, revealing a direct linear correlation between the wear rate and applied load. As the Ti content increases, the wear rate decreases. Notably, the AC2-AC4 alloys exhibit linear wear rate profiles, whereas AC1 displays an accelerated increase above 40 N. The wear rate ranges from $2-92-9.7 \times 10^{-3}$ mm³/m for AC1, $1-6.7 \times 10^{-3}$ mm³/m for AC2, $1-5.2 \times 10^{-3}$ mm³/m for AC3, and $1-4.7 \times 10^{-3}$ mm³/m for the AC4 alloy. Specifically, the AC4 alloy wear rate is 50% less than that of AC1 and 40% and 10% less than those of the AC2 and AC3 alloys, demonstrating its superior wear resistance. Figure 19 (b) shows the variation in the wear rates of the AC alloys with respect to the applied load at 100°C. The results show a significant increase in the wear rate with increasing load for all the alloys. Notably, the wear rates at 100°C are lower than those at room temperature (RT) for all the AC alloys, with a steady decrease in the wear rate as the Ti content increases. At 50 N, the wear rate reduction compared with that at RT is substantial and is 10% for AC1, 11.4% for AC2, 18% for AC3, and 28% for AC4. Wear rates increase gradually between 10–30 N, followed by a rapid increase beyond 30 N. Figure 19(c) shows that at 200°C, the wear rate increases with load for all alloys, with a 7– 10% decrease compared with that at 100°C, indicating temperature-dependent wear behavior. However, under high loads (30–50 N), the AC1, AC2, and AC3 alloys exhibit a sharp increase in the wear rate, deviating from the trend, whereas the AC4 alloy wear rate transitions from mild to high at 30 N. Figure 19(d) reveals a substantial increase in the wear rate with increasing load at 250°C for the AC alloys, surpassing the rates at RT, 150°C, and 200°C. At 50 N, the wear rate at 250°C was nearly double that at 200°C. Although Ti alloying reduces wear rates across temperatures, with decreasing wear rates as the Ti content increases, the trend reverses at 250°C,

where all alloys exhibit markedly high wear rates. Notably, the AC4 alloy has the lowest wear rate. Reductionofthewearratebetween100°Cand200°Casaresultofthedevelopmentofaprotectiveoxidelayer onthealloysurface. Furthermore, the Si particles become less abrasive due to softening at high temperatures, which further reduces the wear rate [36,37].

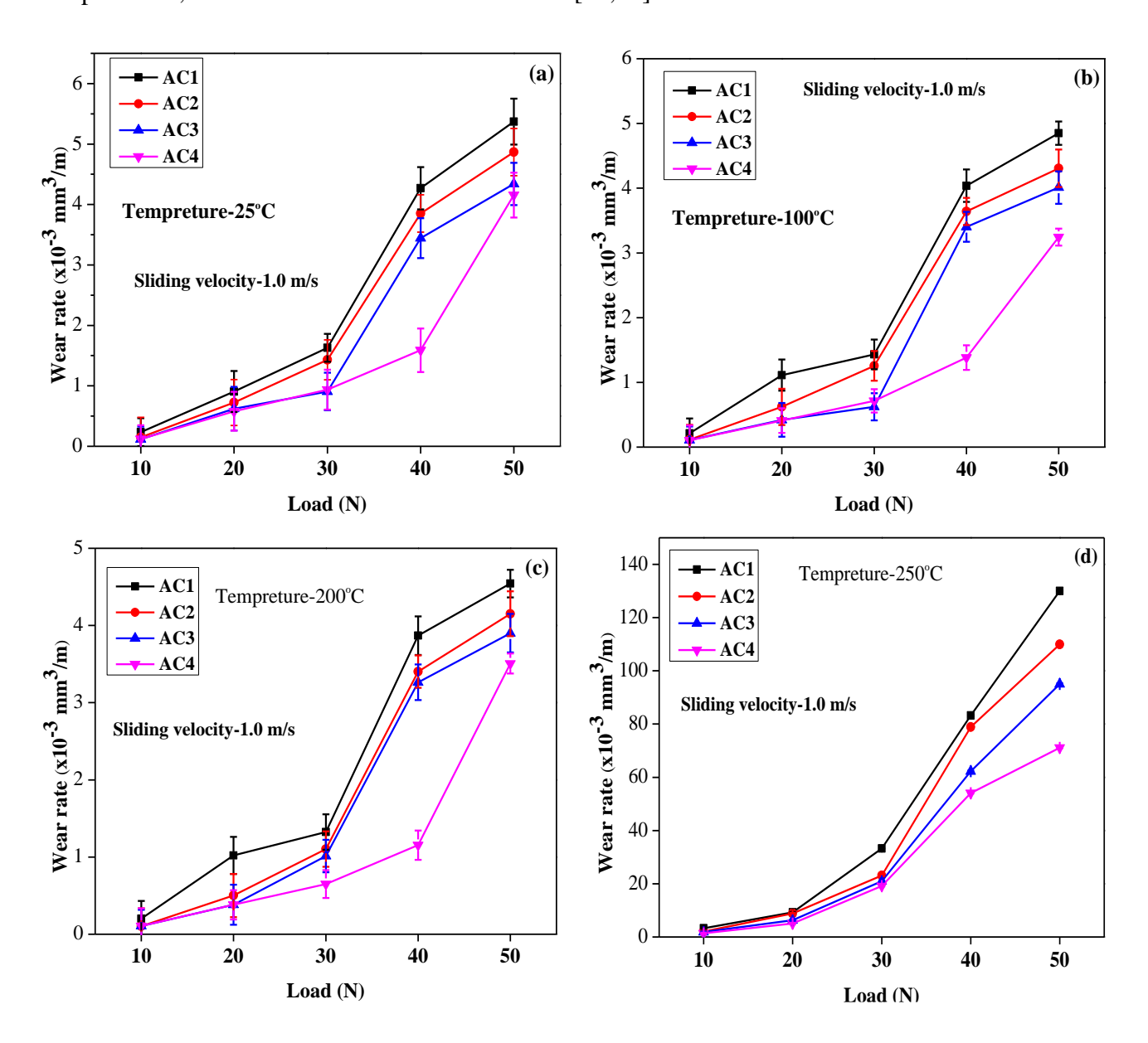


Figure 19. Variation in the wear rate with load of AC alloys at temperatures of (a) 25°C, (b) 100°C, (c) 200°C, and (d) 250°C

In addition, the alloy is hardened by work hardening, which increases its hardness and wear resistance [38]. The reduced wear rate is also partly the result of heat activation of plastic deformation mechanisms such as dislocation sliding and grain boundary sliding [39]. The high silicon content of the alloy provides a strong, abrasion-resistant, silicon-rich coating on the surface, while titanium refines the grain structure and increases wear resistance.

Figure 20 displays the variation in wear rate versus load for the SF1, SF2, SF3, and SF4 alloys at different temperatures. The SF4 alloy consistently exhibited a lower wear rate than the other SF alloys under identical sliding conditions. At room temperature (RT) (Figure 20(a)), the wear rates of the SF1, SF2, SF3, and SF4 alloys are 46.7%, 54%, 53%, and 61.5% lower, respectively, than those of the AC1, AC2, AC3, and AC4 alloys at 50 N. This indicates a 50–65% greater wear rate for the AC alloys than for the SF alloys at RT. At 100°C (Figure 20 (b), the wear rate of the SF4 alloy increases linearly with increasing load, whereas that of the SF alloys (SF1, SF2, and SF3) shows a nonlinear increase with increasing load, with a high positive wear slope above 40 N. Compared with those at RT, all the SF alloys exhibited a significant decrease in the wear rate at 100°C, with 35%, 54%, 57%, and 74% for the SF1, SF2, SF3, and SF4 alloys, respectively, compared with those of the AC alloys at 50 N. Figure 20(c) shows the wear rates of the SF alloys at 250°C, which are lower than those at RT and 200°C. A comparative analysis revealed a significant decrease in the wear rate as the temperature increased from 100 to 200°C, with the wear rates of the SF1, SF2, SF3, and SF4 alloys decreasing by 52%, 39%, 40%, and 28%, respectively. Moreover, the wear rate of the SF alloys is substantially lower than that of the AC alloys by 68%, 71%, 73%, and 82%, respectively. Figure 20(d) shows the wear rate of the SF alloys at 250°C, revealing a significant increase in the wear rate compared with that at lower temperatures. Compared with that at 200°C, the wear rate increases by 26% for SF1, 37% for SF2, 54% for SF3, and 74% for SF4. Above 200°C, the wear rate increases for both the AC and SF alloys, indicating a significant impact of temperature on the wear rate. This study reveals a direct correlation between the wear resistance and applied load of AC and SF alloys. Microstructural refinement, particularly Ti intermetallic particles and a uniform Si phase distribution, significantly enhances the wear resistance. The presence of Ti enhances the transition load, promoting stable protective oxide layers and intermetallic compounds that support the surface oxide layer.

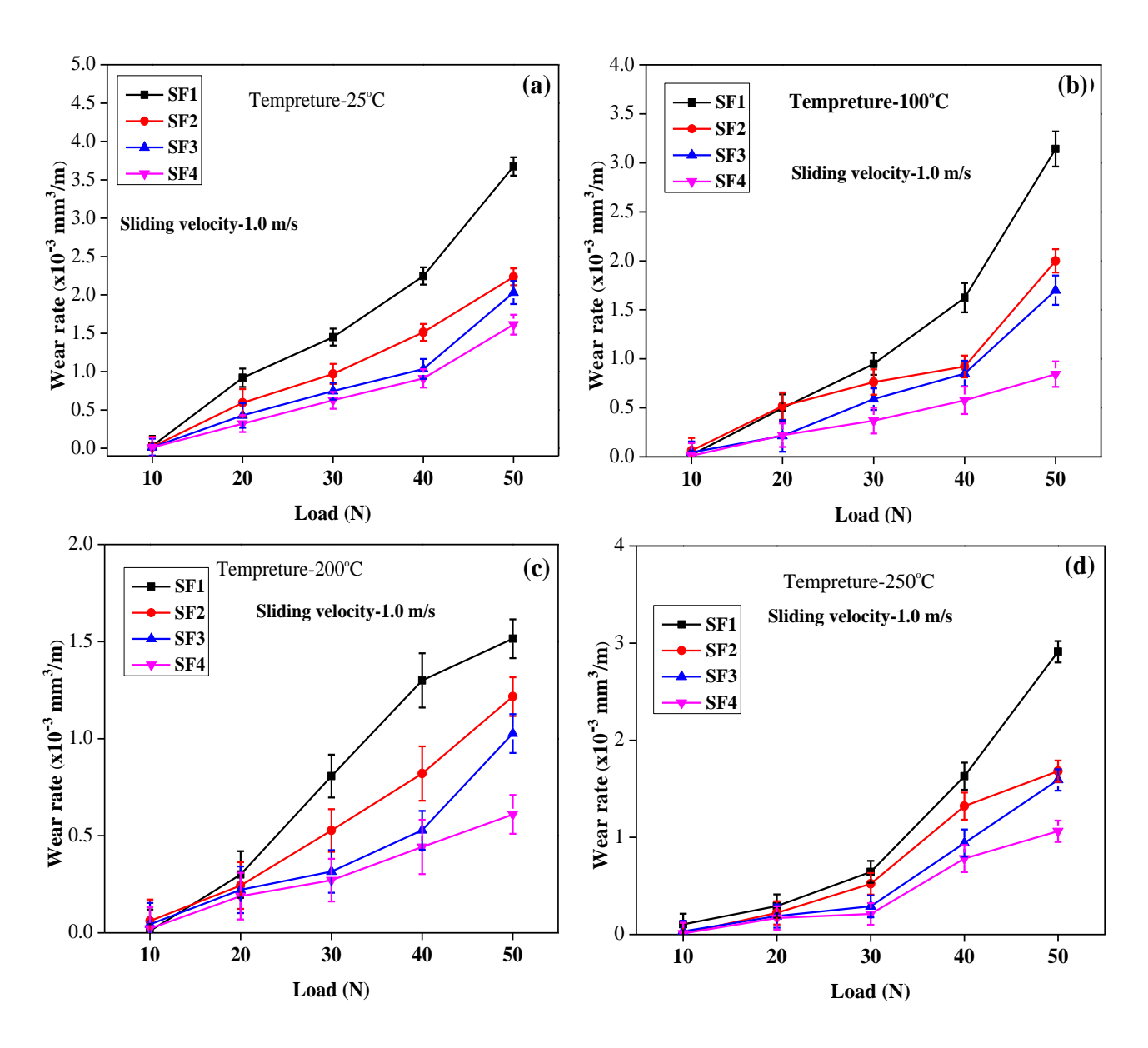


Figure 20. Variation in the wear rate with load of the SF alloys at temperatures of (a) 25°C, (b) 100°C, (c) 200°C, and (d) 250°C

3.4.2. Specific wear rate (k)

The load-carrying capacity of AC alloys, represented by the wear severity (k), is calculated by dividing the volumetric wear rate by the applied load. Figure 21 displays 3D plots of k at various temperatures and loads, showing that k increases with increasing load and decreases with increasing temperature from RT to 200°C. However, at 250°C, the AC alloys exhibit higher k values, indicating a decrease in the load-carrying capacity. The k range for the AC1, AC2, AC3, and AC4 alloys between RT and 200°C indicates that the base alloy has a low load-carrying capacity, which increases with increasing Ti content in the AC alloys. At 250°C, the range k valuesfor the AC1, AC2, AC3, and AC4 alloys are $3.2 \times 10^{-4} - 2.6 \times 10^{-3}$, $2.0 \times 10^{-4} - 2.2 \times 10^{-3}$, $1.8 \times 10^{-4} - 1.910^{-3}$, and $1.41 \times 10^{-4} - 1.42 \times 10^{-3}$ mm³/N-m, respectively, further highlighting the decrease in the load-carrying capacity at elevated temperatures.

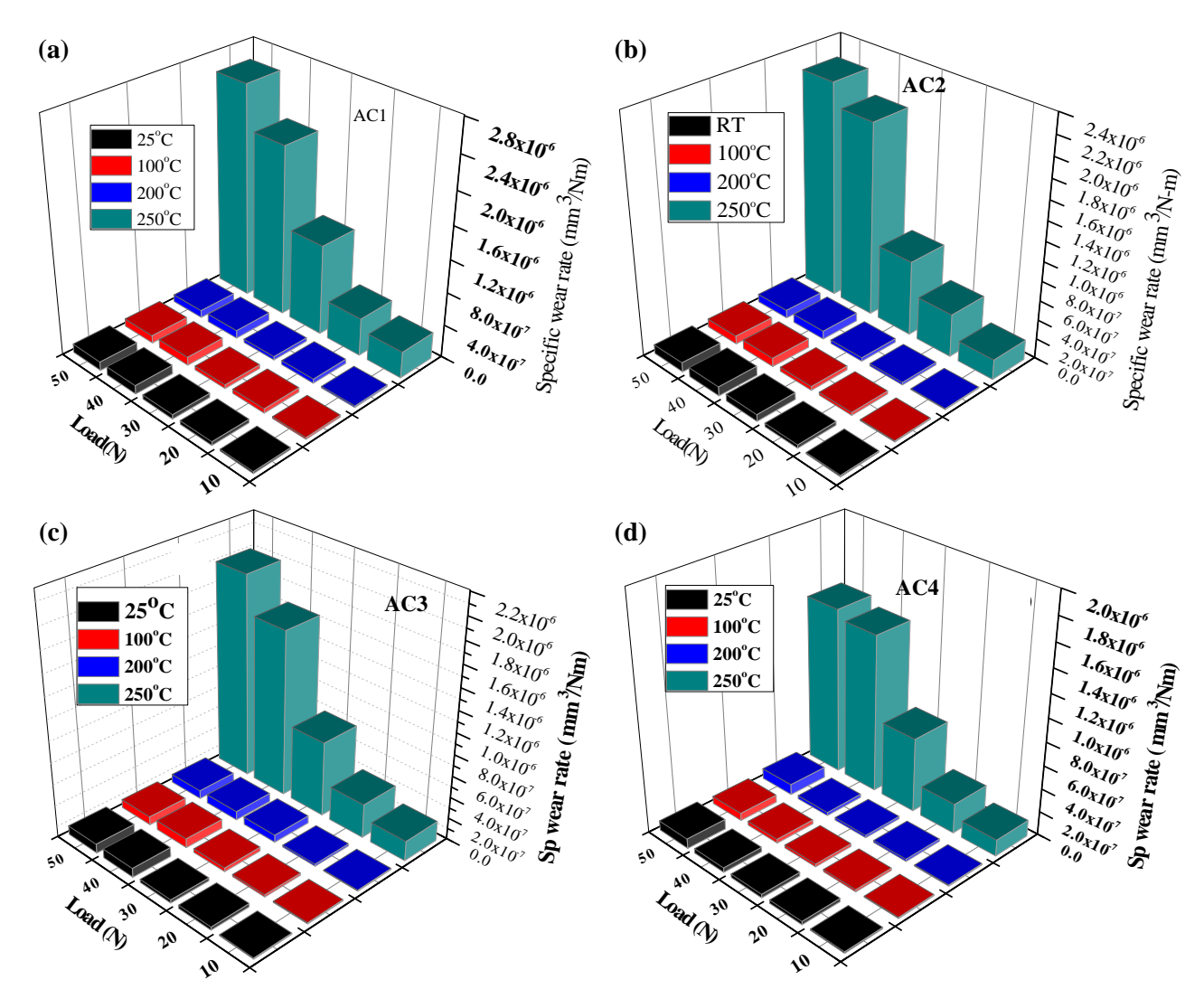


Figure 21. Variation in the specific wear rate with load and temperature for the (a) AC1, (b) AC2, (c) AC3, and (d) AC4 alloys

Figure 22 displays the variation in k with load for the SF alloys at different temperatures, showing a gradual increase in the specific wear rate with load and lower k values than those of AC alloys. SF alloys exhibit a decrease in k with increasing temperature from RT to 200°C, followed by an increase in k with increasing temperature.

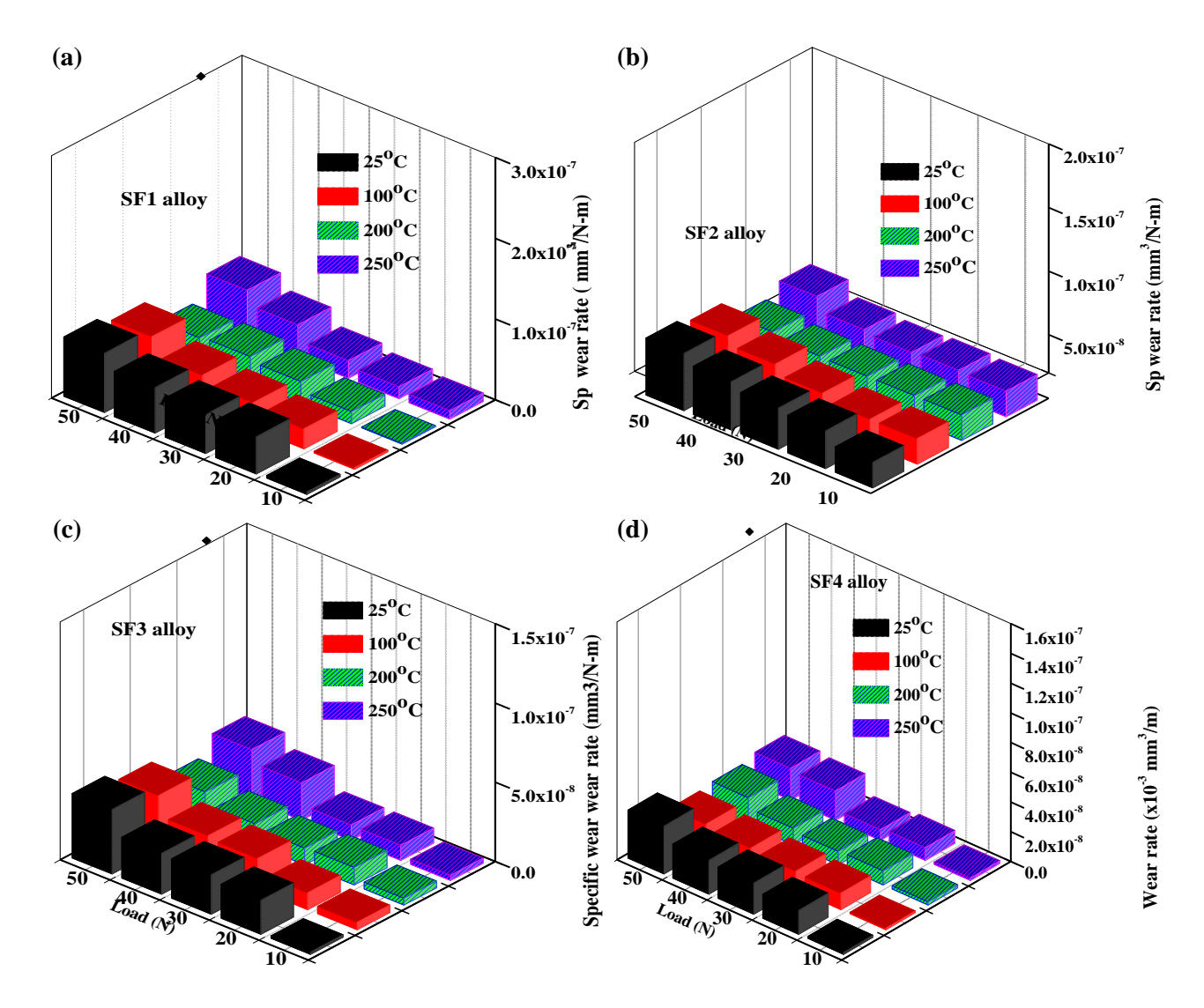


Figure 22. Variation in the specific wear rate with load and temperature for (a) SF1, (b) SF2, (c) SF3, and (d) SF4 alloys

In the load range of N and temperature range from RT to 200° C, the k values for the SF1, SF2, SF3, and SF4 alloys vary from 3.08×10^{-6} to 7.35×10^{-5} , 2×10^{-6} to 3.36×10^{-5} , 1.5×10^{-6} to 3.18×10^{-5} , and 1.23×10^{-6} to 2.12×10^{-5} mm³/N-m, respectively. This demonstrates that the SF4 alloy has a lower k than the SF1, SF2, and SF3 alloys do, indicating a higher load-carrying capacity for SF alloys with a higher Ti content. The presence of Ti in SF alloys enhances their load-carrying capacity, with the SF4 alloy exhibiting the highest capacity because of its high Ti content.

3.4.3. Coefficient of Friction (μ)

Figure 23(a-d) shows the variation in the coefficient of friction (COF) with increasing load (10-50 N) at temperatures ranging from 25°C(RT)-250°C for the AC alloys. The results show a consistent decrease in the COF with increasing load for all the alloys at all the temperatures, accompanied by a significant increase in the COF with increasing temperature. These findings suggest that both the load and temperature influence the frictional behavior of these alloys. At room temperature (RT),

the COF of AC1 (Figure 23 (a)) ranges from 0.57 at 10 N to 0.498 at 50 N. However, the Ticontaining Al-Si alloys (AC2, AC3, and AC4) exhibit lower μ values than AC1, with AC4 showing the lowest COF in the entire load range at RT. Compared with AC1, AC4 results in a 13% reduction in the COF at 10 N and a 9% reduction at 50 N, which decreases gradually with increasing load. The results also show that as the Ti content increases, μ decreases across all loads, indicating a negative correlation between the Ti content and frictional behavior. Compared with AC2, AC3 results in a 3–4% reduction in the COF, whereas compared with AC3, AC4 results in a 1.5–2.8% reduction. At 100°C (Figure 23(b)), μ decreases with increasing load, but the temperature effect is pronounced, with an 8–10% increase in μ for AC1, a 7–12% increase for AC2, an 8–10% increase for AC3, and a 5–10% increase for AC4 compared with the RT values.

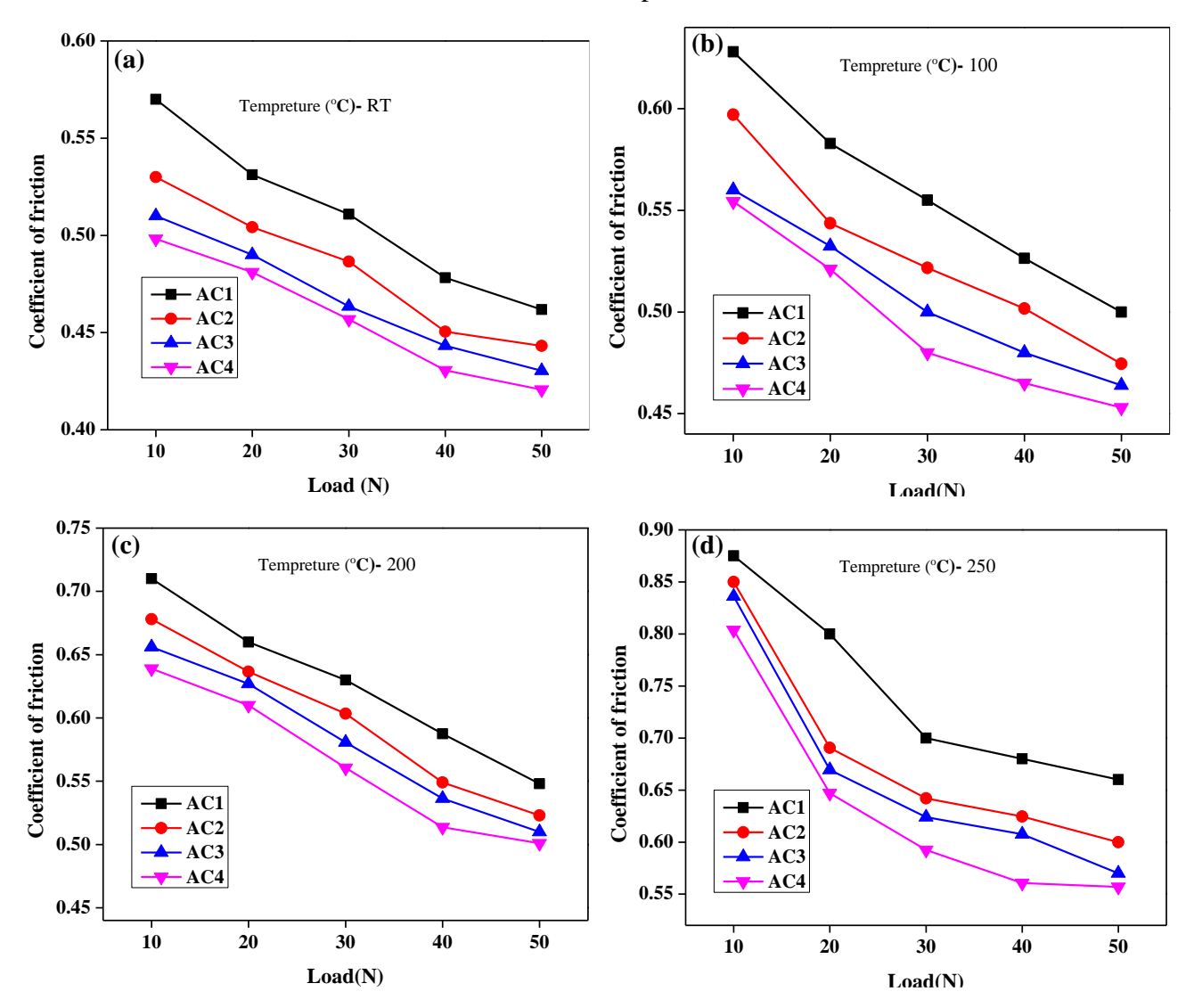


Figure 23. Variation in the coefficient of friction with load for AC alloys at temperatures of (a) 25°C, (b) 100°C, (c) 200°C, and (d) 250°C

At 200°C (Figure 23 (c)), the μ values decrease with increasing load, with a more significant increase in μ (10–13% for AC1, 9.5–15% for AC2, 9.5–17% for AC3, and 9.5–17.5% for AC4)

than at 100° C. At 250° C (Figure 23(d)), the COF decreases with increasing load, with a significant decrease in the low load range (10–20 N) and a high negative slope rate of μ with increasing load. Compared with those at 200° C, there was a notable increase in μ at 250° C: 23% at 10 N and 20% at 50 N for AC1, 25% at 10 N and 14% at 50 N for AC2, 27% at 10 N and 12% at 50 N for AC3, and 26% at 10 N and 11% at 50 N for AC4. Throughout the entire load range (10–50 N) and temperature range (RT– 250° C), the AC4 alloy exhibited lower μ values than did AC1, AC2, and AC3.

Figure 24 shows the variation in μ with load for the SF alloys, with a consistent decrease in μ with increasing load for all the SF alloys. The SF4 alloy had the lowest average COF, whereas the SF1 alloy had the highest value, followed by SF2 and SF3. Notably, the μ values for the SF alloys are consistently lower than those for the AC alloys at all loads and temperatures.

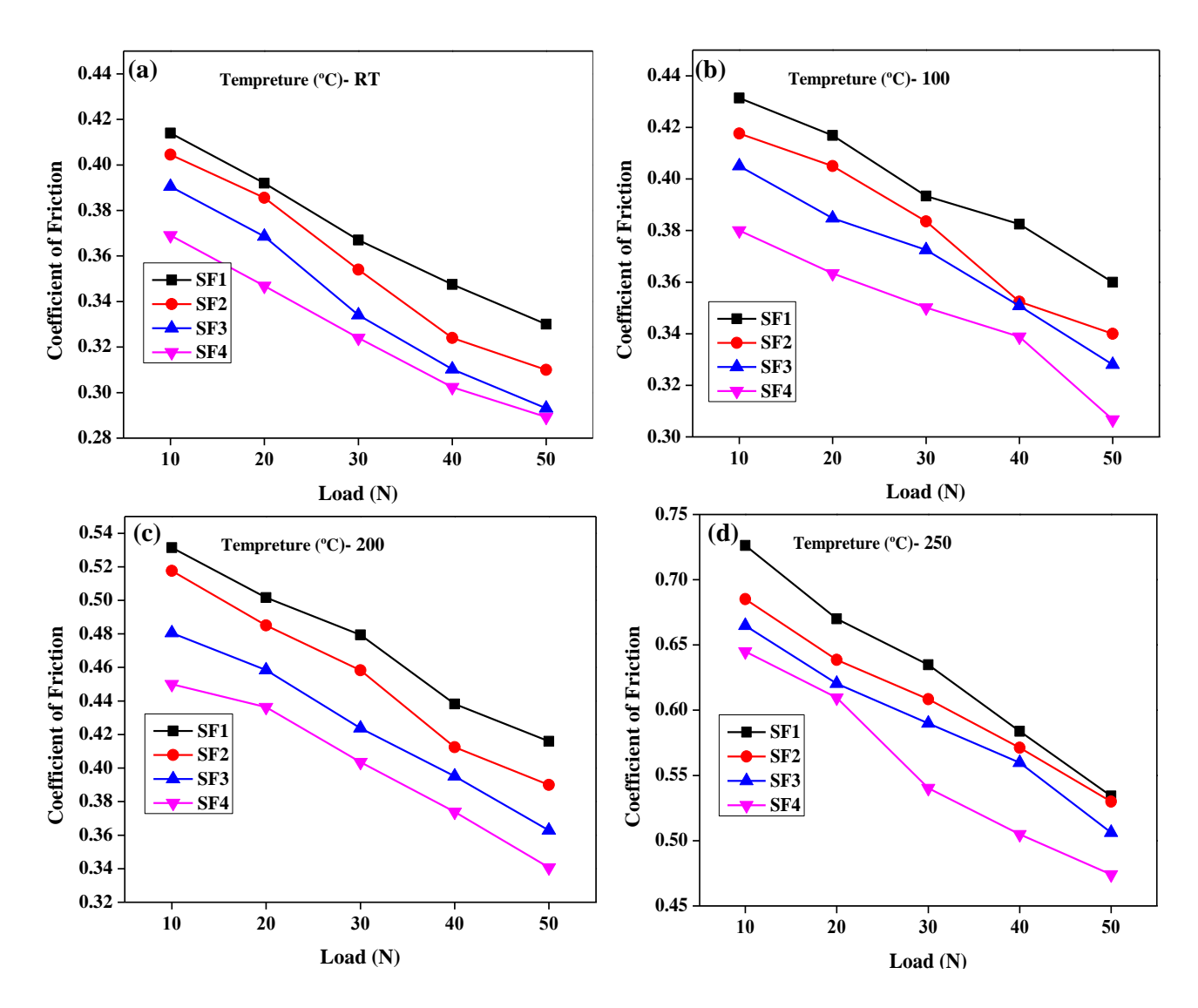


Figure 24 Variation in the coefficient of friction with the load of SF alloys at different temperatures (a) 25°C, (b) 100°C, (c) 200°C, and (d) 250°C

A comparative study at RT (25°C) (Figure 24 (a)) revealed a significant reduction in the COF for the SF alloys, with a 39% reduction for SF1, 42% for SF2, and 46% for both SF3 and SF4, compared with those of the AC alloys. At 100° C (Figure 24 (b)), the COF increases for SF alloys, with a 4–9% increase at 10 N and 50 N for SF1, 3–9% for SF2, 3–13% for SF3, and 3–12% for SF4, compared with the RT values. Compared with those at 100° C, the μ values at 200° C (Figure 24 (c)) are lower for SF alloys than for AC alloys, with a 23-15% reduction at 10 N and 50 N for SF1, 24–14% for SF2, 19–11% for SF3, and 18–10% for SF4. At 250° C (Figure 24 (d)), μ increases sharply with increasing load, with a 36-28% increase for SF1, 31-36% for SF2, 35-41% for SF3, and 35-40% for SF4 at 10N and 50 N, compared with that at 200° C.

Figure 25(a-d) displays representative 3D plots of AC alloys, illustrating the variation in μ with load and temperature (25–250°C). The μ value increases with temperature and decreases with load. The μ of AC1 at RT (Figure 25(a)) significantly changes with temperature, with a similar trend observed for the AC2, AC3, and AC4 alloys (Figure 25(b-d)). The increase in μ values per unit rise in temperature at 10 N is 35% for AC1, 34% for both AC2 and AC3, and 33% for AC4. Additionally, μ increases by 26.4% for AC1, 24% for AC2, 22.8% for AC3, and 21% for AC4 per unit temperature increase at 50 N.

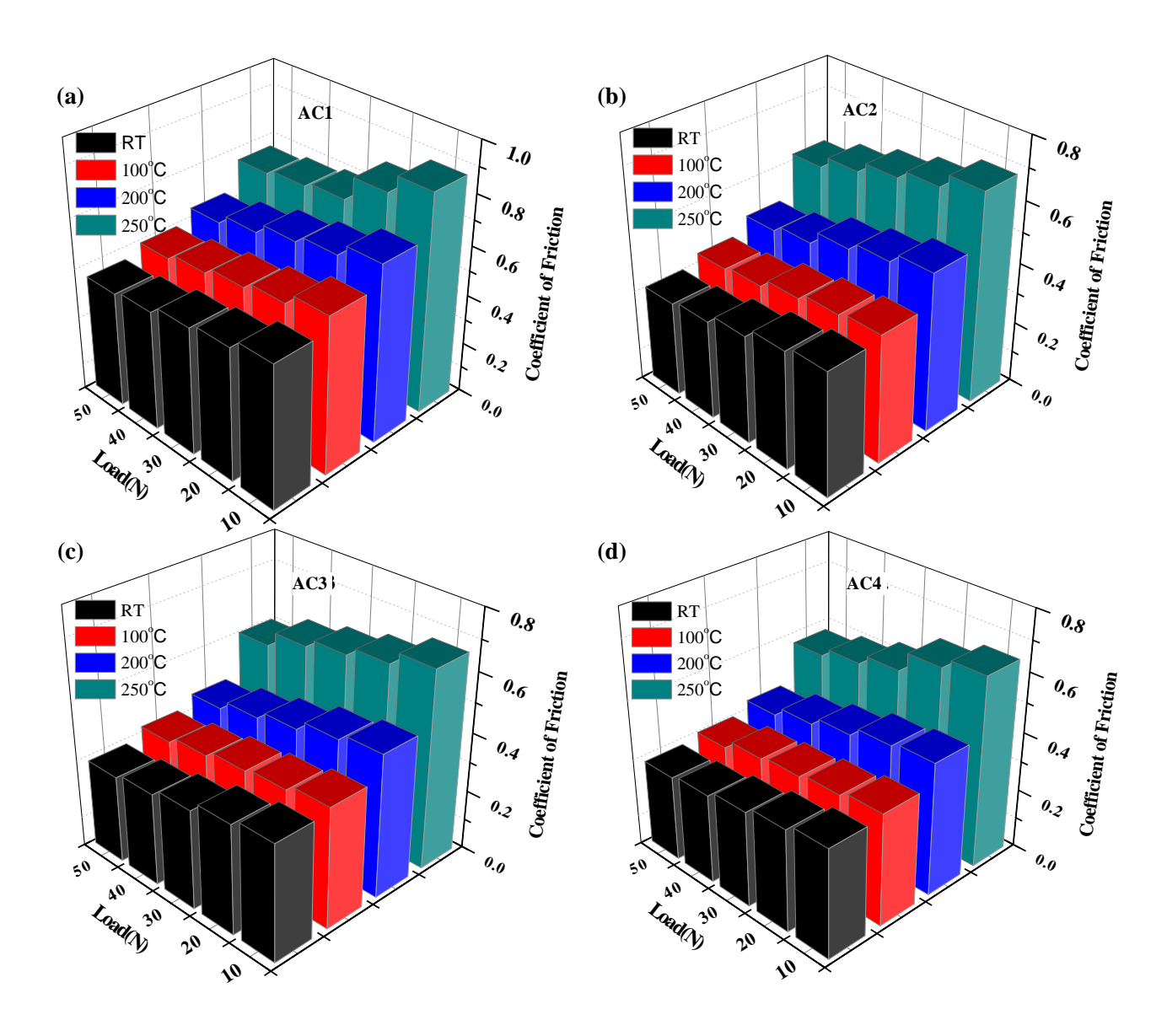


Figure 25. 3D plots of AC alloys showing the variation in the COF with load and temperature for (a) AC1, (b) AC2, (c) AC3 and (d) AC4 alloys.

Figure 26 displays 3D plots of the SF alloys, illustrating the effects of load and temperature on μ . A consistent trend of decreasing μ with load and increasing μ with sliding temperature is observed. The SF4 alloy has the lowest μ throughout the applied load and temperature range, with μ values less than those of the AC alloys. A comparative study revealed that the increase in μ per unit increase in temperature at a 10 N load was 0.29% for SF1, 0.27% for SF2, 0.26% for SF3, and 0.25% for SF4, and at a 50 N load, it was 0.22% for SF1, 0.21% for SF2, 0.20% for SF3, and 0.18% for SF4. Notably, the SF4 alloy has a lower μ than the SF1, SF2, and SF3 alloys across the entire applied load range (10–50 N) and temperature range (RT–250°C).

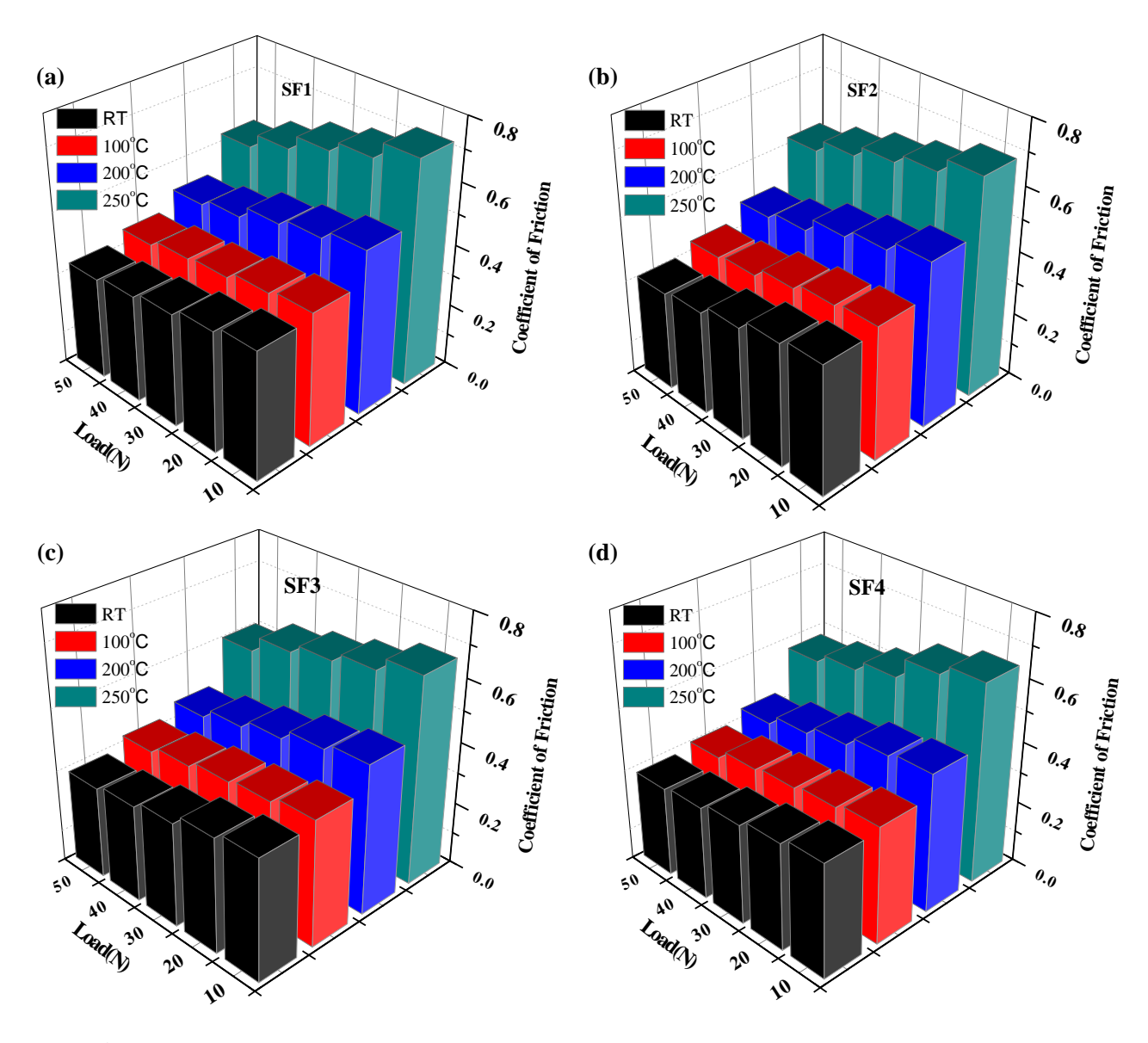


Figure 26. 3D plots of SF alloys showing the variation in the COF with load and temperature for (a) SF1 (b) SF2 (c) SF3 and (d) SF4 alloys.

Compared with that of AC alloys, the superior wear resistance of SF alloys is attributed to the uniform and fine distribution of primary Si phases in the Al matrix. During wear testing, Si- and Tirich intermetallic phases undergo extensive fracturing, particularly in the coarse Si, flake, and needle-like phases. An increased Si content, shear stress, Si size, and intermetallic size amplify fractures [40]. Localized deformation near Si and intermetallic phases leads to stress concentration, which is influenced by the phase size. Coarse Si phases and intermetallics experience greater stress concentrations, facilitating easier fracturing and reducing wear resistance. In contrast, fine Si phases and intermetallic particulates enhance the wear resistance [41]. The obtained coefficient of friction (μ) values align with those of previous research [42]. The microstructural characteristics and Ti content significantly impact the μ and wear behavior [43]. Notably, increasing the Ti content from 0.5 wt.% to 2 wt.% substantially reduces the wear rate and μ . At low loads, oxidation and adhesion prevent direct metallic contact, minimizing metal–metal interactions. As the load increases, μ

decreases, indicating complete metallic contact and eliminating surface asperity locking. The coefficient of friction (μ) varies minimally at higher loads because aluminum (Al) is the dominant component in all alloys. At high loads, the Al matrix in the sample and counter face directly contacts each other, dictating the effective μ . Frictional behavior is influenced by the actual contact area between surface asperities, driven by plastic deformation, cold welding, applied load, and hardness.

The relationship between the COF and temperature is expressed by equation (3)[44].

$$\mu = \Delta T. \, 8k. \, (3\pi\sigma_{\nu})^{-1/2} (W)^{-1/2} (v)^{-1} \tag{3}$$

where ΔT represents the change in temperature, k represents the thermal conductivity of the material, v represents the sliding speed, W represents normal load and σ_y the yield stress of the material.

The equation shows that the coefficient of friction (μ) decreases with increasing normal load. Conversely, equation (3) indicates that μ increases with temperature. This aligns with the established knowledge that μ is inversely proportional to metal hardness. Harder metals undergo less plastic deformation, reducing adhesion and metal-to-metal friction. These findings are consistent with existing research on the effects of loading and alloying additives on μ , reinforcing the understanding of frictional behavior [45].

3.4.4. Wear surface topography

The worn-out surfaces of the AC and SF alloys were analyzed to determine the dominant wear mechanism at 50 N and 250°C. Figure 27 (a) shows the wear morphology of the AC1 alloy at 250°C, which is characterized by extensive plowing, wear scars, crater and pit formation, large dimples, and ridging. This severe wear is attributed to the embrittlement and micro cracking of coarse Si phases, which leads to particle—matrix separation and debris-induced damage. As a result, the alloy exhibited deep, irregular grooves due to the synergistic effects of this wear mechanism. Figures 27(b-d) illustrate the distinct wear characteristics of the AC2, AC3, and AC4 alloys. The AC2 alloy exhibited shallow grooves and scratches with fractured oxide layers, indicating reduced surface damage. In contrast, AC3 shows pronounced plowing and shearing marks, plastic deformation, and material transfer, which are characteristic of adhesive wear. AC4 displays abrasive scoring marks, wider craters, and narrow grooves, indicating that third-body abrasives and trapped hard Si particles promote surface damage through abrasive wear, distinguished by narrow grooves without dimples.

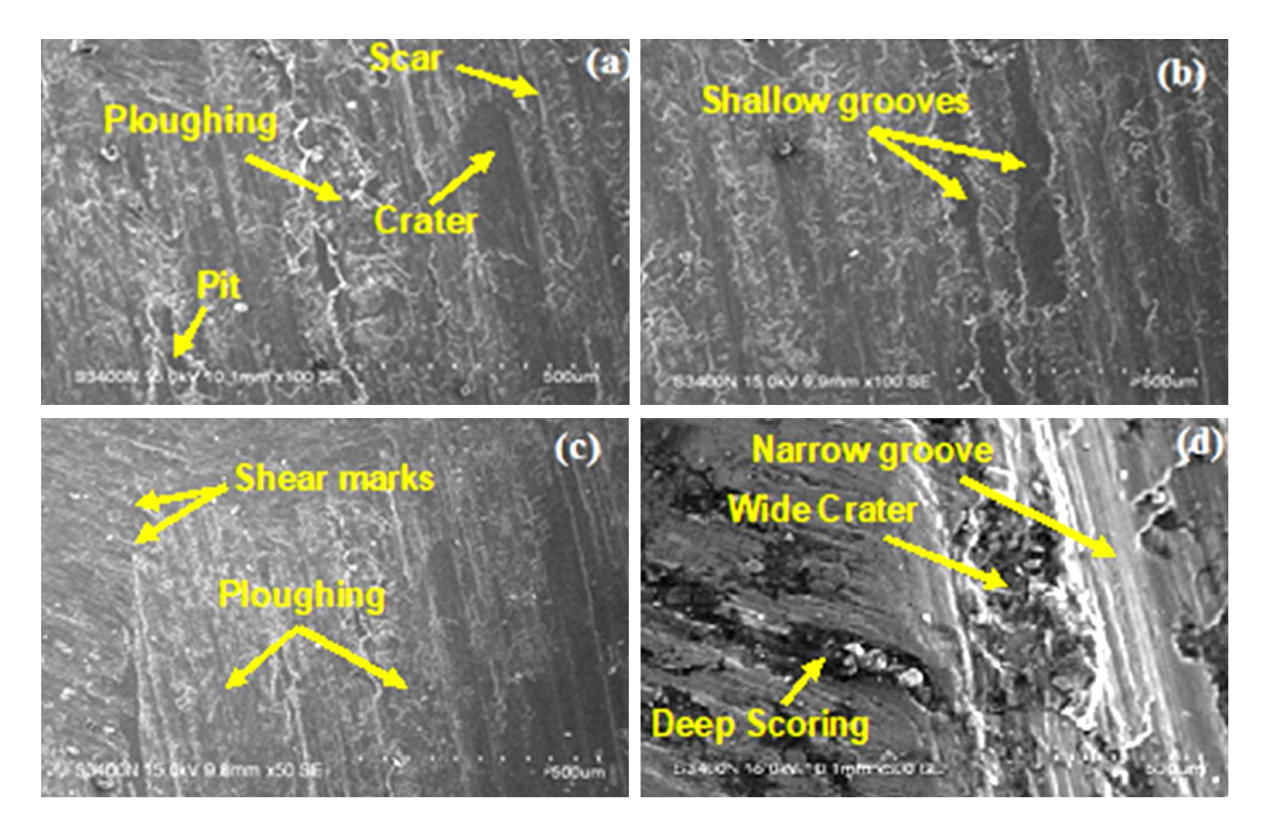


Figure 27. Worn surfaces of AC alloys by SEM at 50 N and 250°C: (a) AC1, (b) AC2, (c) AC3, and (d) AC4

Figures 28 (a-d) illustrate the worn-out topographies of the SF1, SF2, SF3 and SF4 alloys. The SF1 alloy wear surface (Figure 28 (a)) features fine abrasion grooves, few dimples, few scoring marks, and white patches on a relatively smooth surface. In contrast, the SF2 alloy (Figure 28(b)) exhibited shallow, uniform grooves and a smooth surface with fine scoring marks but no pits or dimples, resulting in a low wear rate. Compared with SF1 and SF2, the SF3 alloy (Figure 28(c)) has a relatively smooth surface with shallower grooves and reduced surface roughness. The SF4 alloy (Figure 28 (d)) has a smooth surface with medium scoring marks, small grooves accompanied by plastic deformation, and oxidized asperities. Despite this, the damage is less severe, with shallower valleys and peaks than that of SF3.

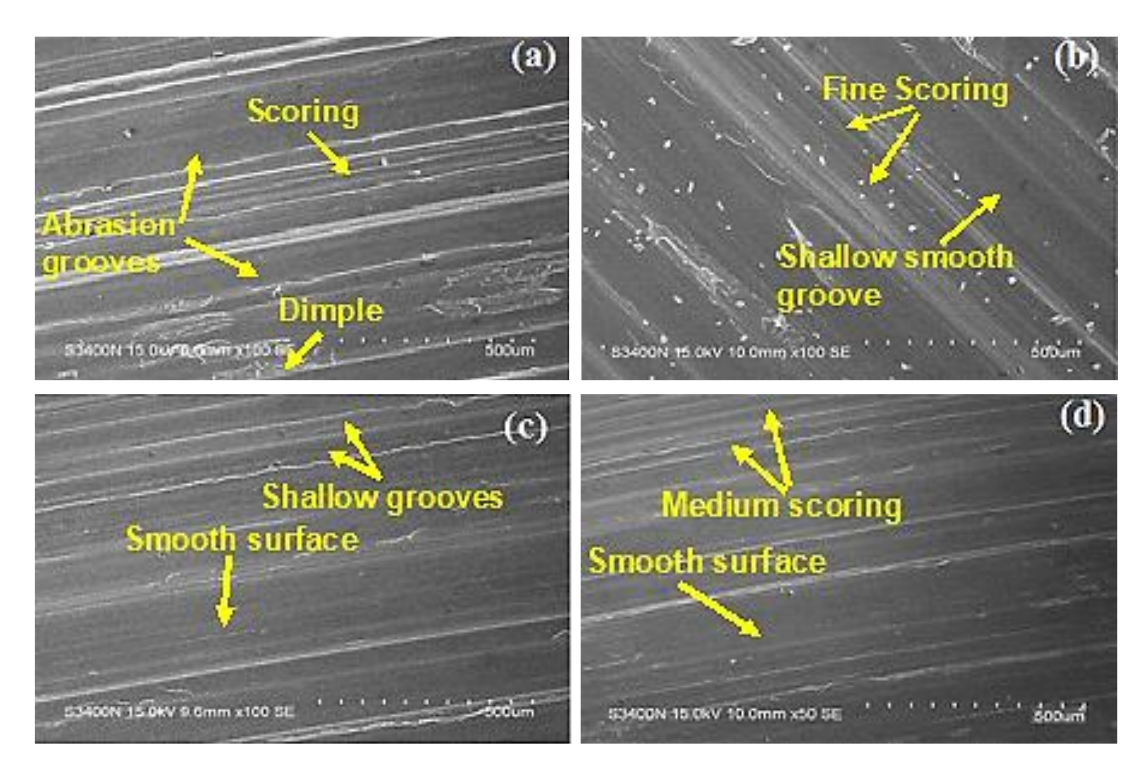


Figure 28. Worn surfaces of the SF alloys observed via SEM at 50 N and 250°C: (a) SF1 (b) SF2, (c) SF3 and (d) SF4 alloys.

3.4.5. Wear debris analysis

The formation of wear particles occurs through the accumulation of residual stress and energy transfer from repeated surface interactions, surpassing the work of adhesion and causing material detachment. Figure 29 (a-d) presents SEM images of the resultant wear debris for AC1-AC4 alloys under 50 N at 250°C, characterized by laminates, flakes, microchips, agglomerates, metallic strings, and fine metal oxides. This diverse morphology suggests a combination of wear mechanisms, including oxidative, abrasive, adhesive, and delamination wear. The morphology of the debris particles reveals delamination and severe metallic wear due to physical failure, as evidenced by long metallic chips. Notably, the AC4 alloy exhibited significantly less wear debris than its counterparts (AC3, AC2 and AC1).

Figure 30(a-d) shows SEM micrographs of wear debris formation in the SF alloys at 50 N and 250°C. Wear debris exhibit an equiaxed morphology with occasional plate-like particles. The appearance of metal oxide powder debris. The small particles in the wear track prove that the wear is both oxidative and abrasive. Distinctively, the SF4 alloy wear particles (Figure 30 (d)) primarily comprise fine metallic particles and large lumps of fine oxide powders, which appear in white contrast, indicating dominant oxide wear.

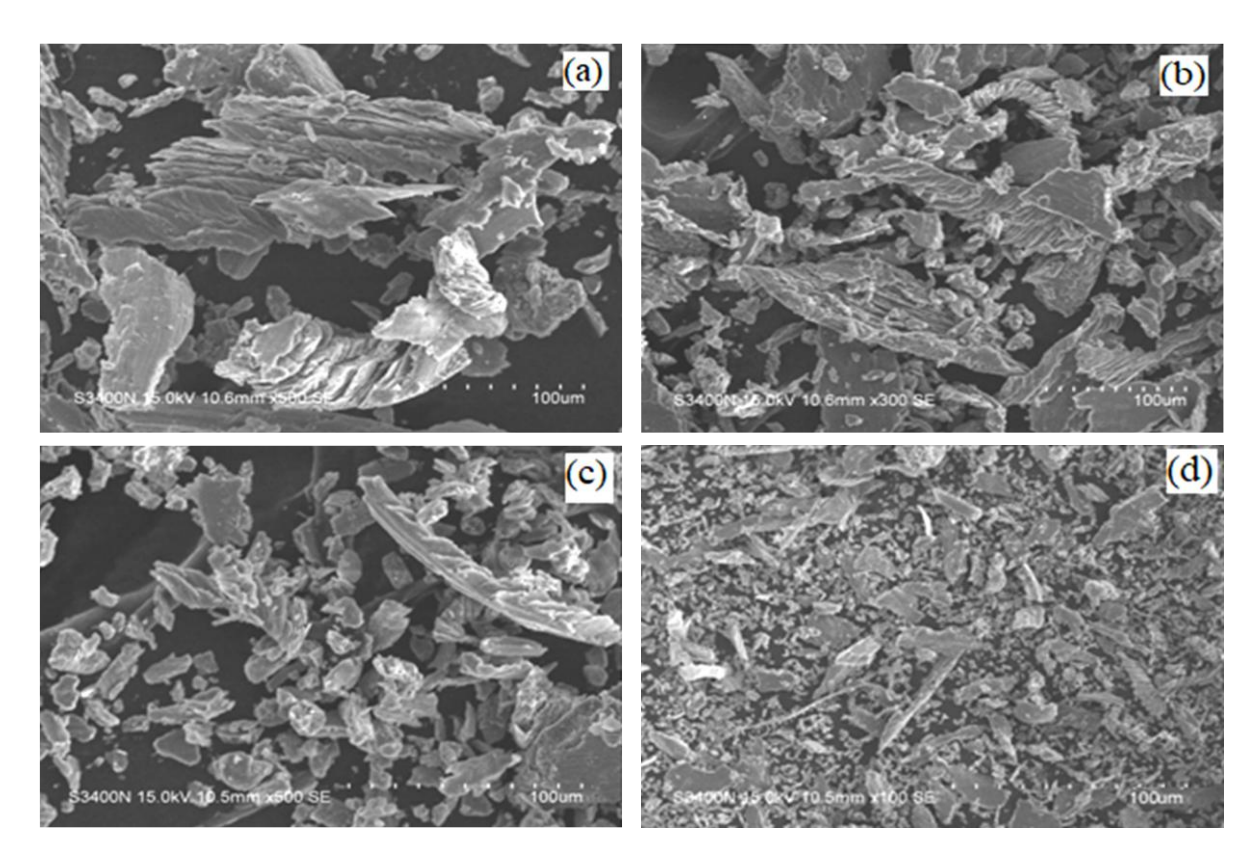


Figure 29. SEM micrographs of wear debris at 250°C and 50 N for the (a) AC1, (b) AC2, (c) AC3 and (d) AC4 alloys

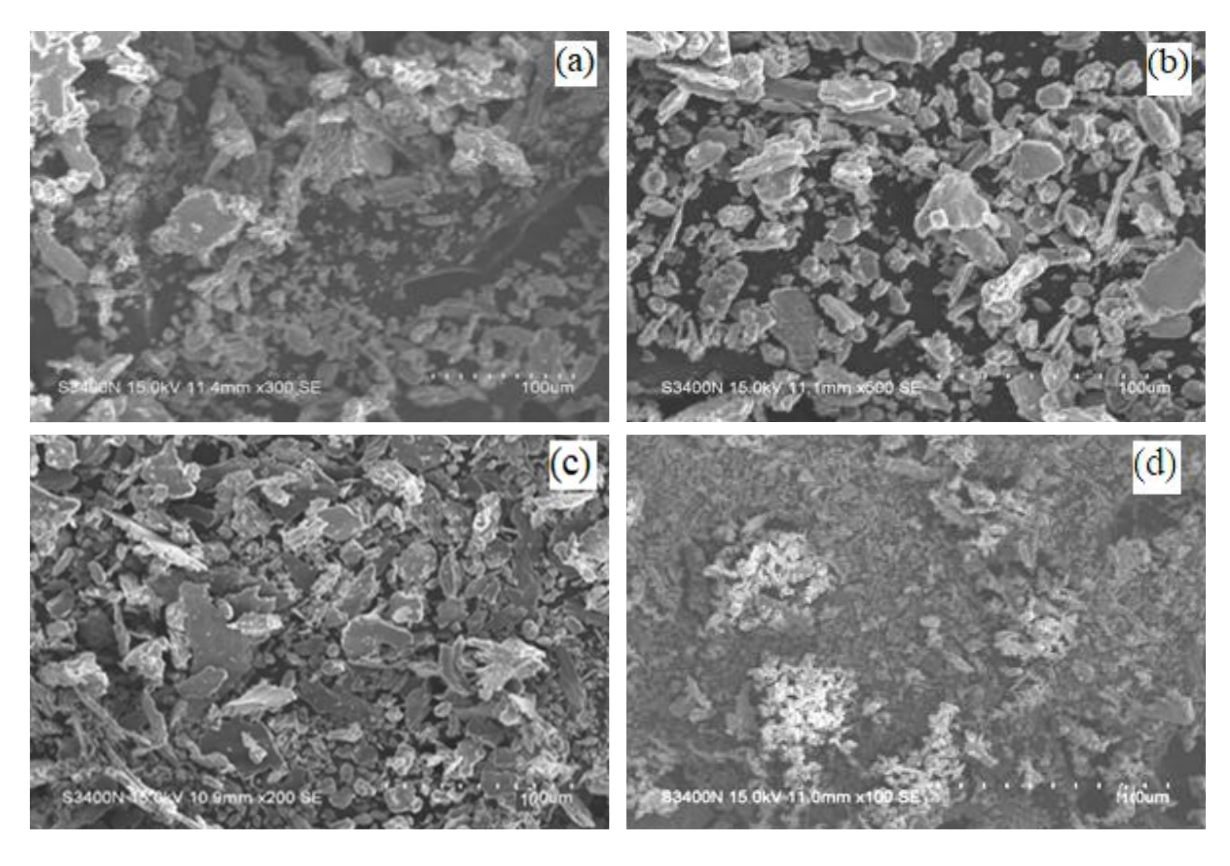


Figure 30. Morphology of the wear debris of the (a) SF1, (b) SF2(c) SF3, and (d) SF4 alloys at 250° C and 50 N

The relationships among the debris size (R), material hardness (H_v) , and applied load (W) are expressed in [46].

$$R = K\left(\frac{W}{H_{\nu}}\right) \tag{4}$$

where R = debris size, K = constant, W = applied load, and $H_v =$ material hardness.

According to equation (4), materials with lower $\left(\frac{W}{H_v}\right)$ ratios produce smaller wear particles, whereas materials with higher $\left(\frac{W}{H_v}\right)$ ratios exhibit larger wear particles. In this study, the AC alloys, which have a lower hardness and higher $\left(\frac{W}{H_v}\right)$ ratios, produce more wear debris. In contrast, the SF alloys, which have a higher hardness and lower $\left(\frac{W}{H_v}\right)$ ratios, produce less wear debris. The $\left(\frac{W}{H_v}\right)$ ratio increases with temperature as the hardness decreases at higher temperatures, resulting in larger wear particles.

3.4.6. Wear mechanism transition map

Wear regime maps provide a comprehensive framework for understanding the complex interactions influencing wear behavior, enabling optimal operating condition identification and material selection for reduced wear and improved performance. These maps were constructed on the basis of the worn surface topography, debris characteristics (size, shape, color), and k values. The wear regimes categorize material behavior according to the specific wear rate, offering insights into material degradation and interaction under various conditions. The specific wear rates vary significantly with material type, surface finish, lubrication, temperature, and load. Common wear regimes are classified on the basis of k values, as established in the literature [47]. Wear regimes are classified on the basis of k values: adhesive wear ($k > 10^{-4} \text{ mm}^3/\text{Nm}$), severe flow wear ($10^{-6} \text{ to } 10^{-5} \text{ mm}^3/\text{Nm}$), mild flow wear ($10^{-6} \text{ to } 10^{-7} \text{ mm}^3/\text{Nm}$), and oxidative wear ($10^{-6} \text{ to } 10^{-5} \text{ mm}^3/\text{Nm}$). Mild wear is controlled by oxidation, whereas severe wear is due to adhesive and abrasive wear resulting from delamination and plastic deformation [48].

Figure 31 shows the relationships between the applied load, temperature and wear regime for the AC alloys. The AC1 alloy exhibited mild wear at loads of 10–20 N and temperatures between RT–200°C, transitioning to oxidative and abrasive wear at 200–250°C. At higher loads (20–50 N) and temperatures (RT–200°C), the wear mechanism shifts to oxidative and abrasive wear. At 50 N and 200–250°C, severe wear occurs due to adhesive and plastic flow. In Ti-based AC2, AC3, and AC4 alloys, mild wear occurs at loads of 10–40 N, with a significant increase in severe wear occurring at loads of 45–50 N, which is attributed to rigid Ti intermetallic phases. A comparison of the wear maps for the AC alloys reveals that the AC4 alloy has a greater mild wear regime and a lower severe and adhesive wear regime.

Figure 32 shows the wear transition map for the SF alloys, which shows the relationships among the load, temperature and wear regime. The SF1 alloy exhibits oxidative wear at loads of 10–30 N and temperatures between RT–250°C, transitions to both oxidative and abrasive wear at high temperatures (200–250°C) and low loads, and severe wear at high loads (45–50 N) and temperatures (RT–250°C). The wear mechanism involves adhesive and plastic flow, leading to severe wear. Ti-based SF2, SF3, and SF4 alloys exhibit oxidative wear at loads of 10–40 N, mild wear at loads of 15–35 N, and temperature-dependent abrasive wear at loads of 45–50 N. Compared with SF1, these alloys exhibit increased oxidative wear and reduced severe wear, attributed to rigid Ti intermetallic phases. The wear maps for the SF alloys show minimal severe wear and dominant oxidative wear modes across the entire temperature range (25–250°C), with high wear resistance at all loads (10–50 N).

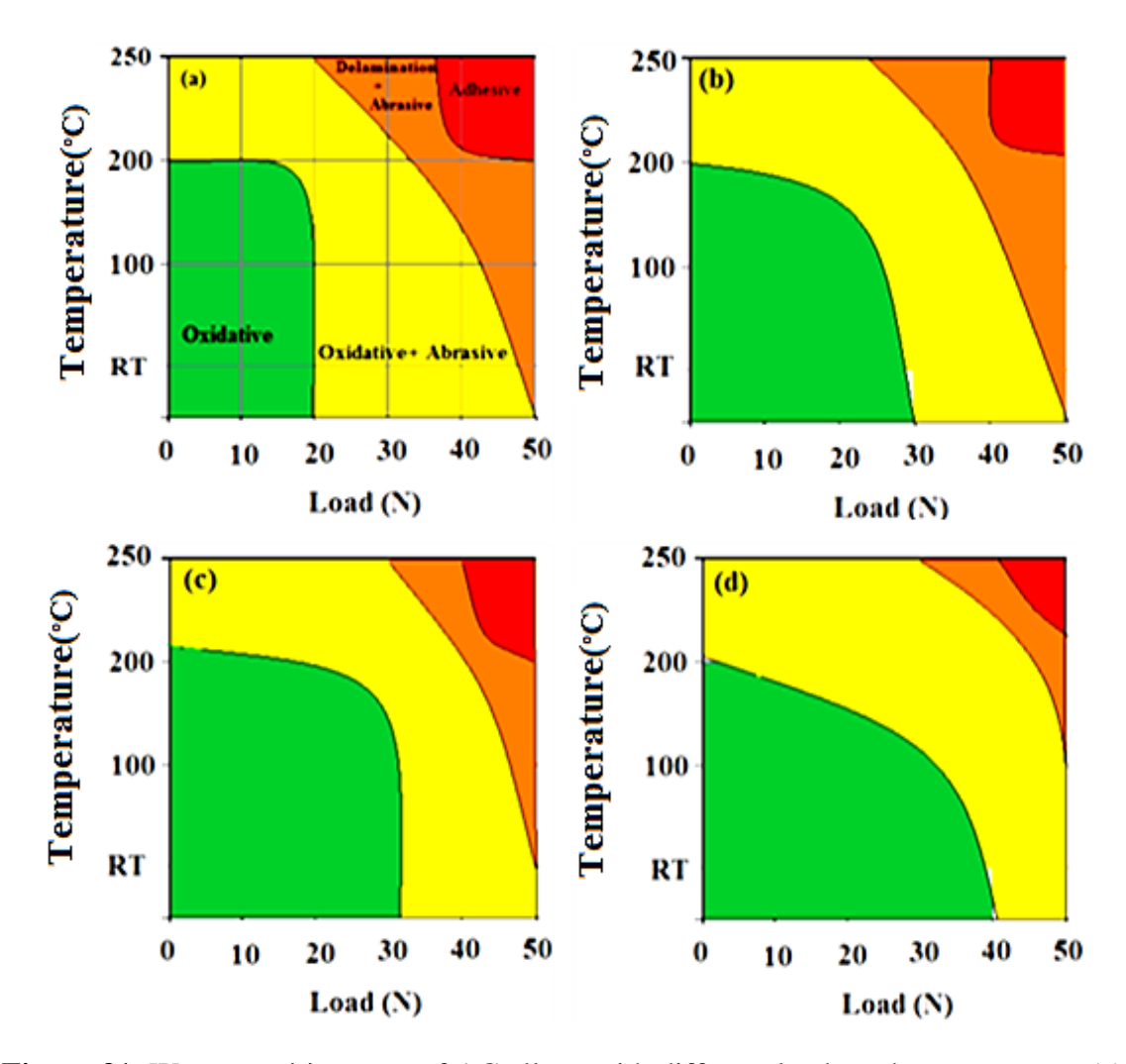


Figure 31. Wear transition map of AC alloys with different loads and temperatures: (a) AC1, (b) AC2, (c) AC3, and (d) AC4

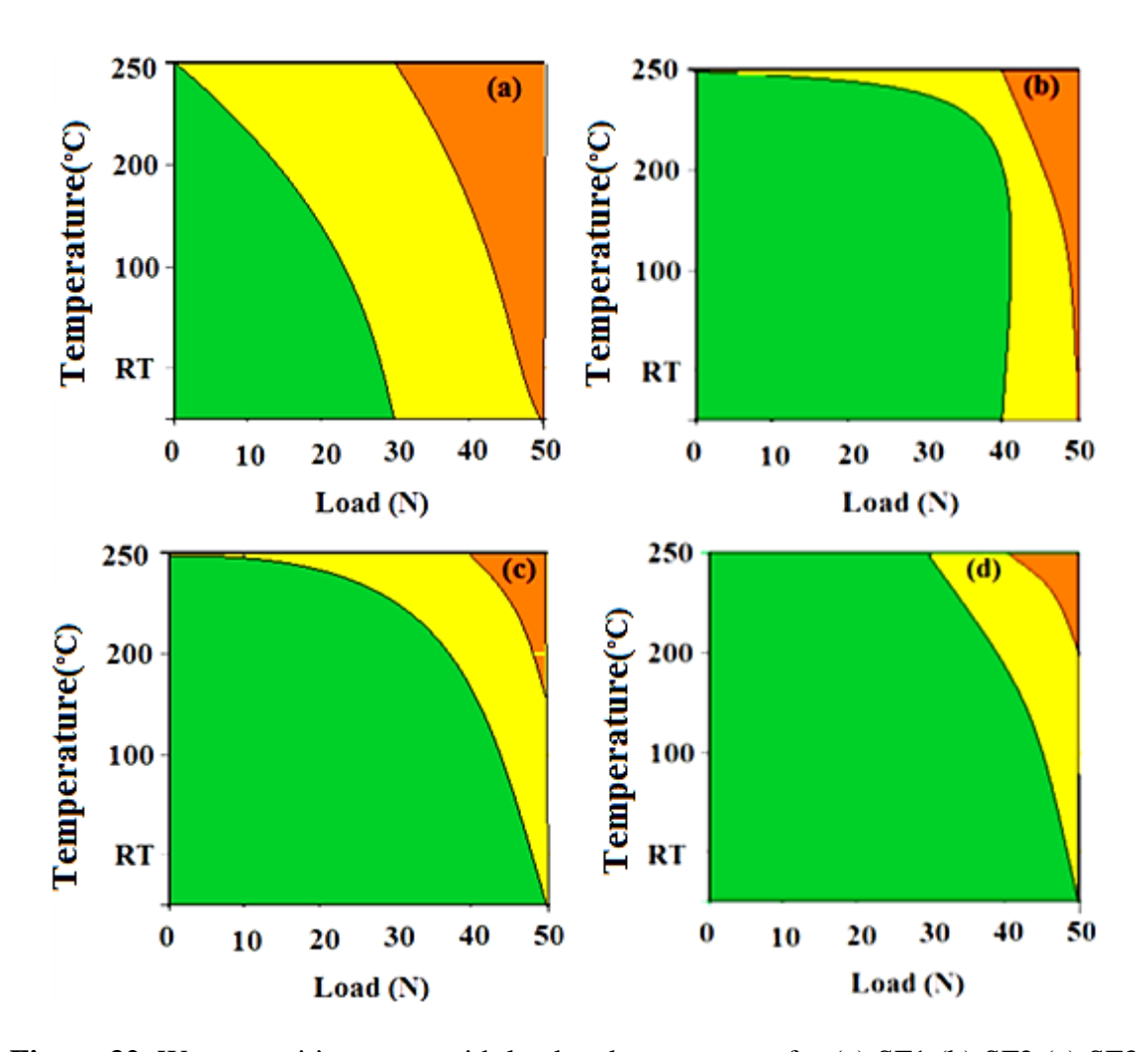


Figure 32. Wear transition maps with load and temperature for (a) SF1 (b) SF2 (c) SF3 and (d) SF4 alloys

4. Conclusions

The microstructure of the spray-formed refined Al-15Si-(0.5-2.0) Ti alloy produced fine, spherical primary Si (3–10 μ m), fine eutectic Si, and uniform Ti-rich intermetallic (~15 μ m) particles in an equiaxed Al matrix. This contrasts with the coarse and irregular microstructures in the corresponding as-cast alloys.

Spray formation significantly enhanced the properties of the Al-15Si-Ti alloys, resulting in 15–46.4% greater hardness from room temperature to 250°C, 41–54% lower wear rates than those of spray-formed Al-15Si, and consistently lower coefficients of friction across 10–50 N loads and from room temperature to 250°C. Notably, the optimized SF4 alloy exhibited significantly lower friction than did the SF1, SF2 and SF3 alloys, with a reduced temperature sensitivity of 0.2 to 0.3% in terms of the coefficient of friction increase per unit temperature increase.

The cast and spray-formed alloys exhibited similar wear mechanisms, including oxidative, abrasive, and delamination wear. However, severe plastic deformation was uniquely observed in the cast alloys, highlighting the distinct differences in wear behavior between the two processing methods.

Acknowledgments

The authors would like to thank VGST, Karnataka State Government for supporting the current research under the scheme of KFISTL1 (2019--20/2020--21).

Declarations

Competing interest: The authors declare that they have no known competing financial interests or personal relationships that could have appeared to influence the work reported in this paper.

Funding: This research received no specific grant from any funding agency in the public, commercial, or not-for-profit sectors.

References

- 1. Stojanovic, Blaza, MilanBukvic, and Igor Epler. "Application of aluminum and aluminum alloys in engineering." Applied Engineering Letters: Journal of Engineering and Applied Sciences (2018). doi.org/10.18485/aeletters.2018.3.2.2
- 2. Shivanath, R., and Eyre TS. "Wear of aluminum-silicon alloys." (1977).
- 3. Miladinović, Slavica, et al. "Hypereutectic aluminum alloys and composites: a review." Silicon 15.6 (2023): 2507-2527. doi: 10.1007/s12633-022-02216-2
- 4. Ejiofor, J. U., and R. G. Reddy. "Developments in the processing and properties of particulate Al-Si composites." Jom 49 (1997): 31-37.
- 5. Callegari, Bruna, Tiago Nunes Lima, and Rodrigo Santiago Coelho. "The influence of alloying elements on the microstructure and properties of Al-Si-based casting alloys: a review." Metals 13.7 (2023): 1174. doi: 10.3390/met13071174
- 6. Elliott, R. "Eutectic solidification." Materials Science and Engineering 65.1 (1984): 85-92.
- 7. Shaha, S. K., et al. "Microstructure and mechanical properties of Al–Si cast alloy with additions of Zr–V–Ti." Materials & Design 83 (2015): 801-812. doi: 10.1016/j.matdes.2015.05.057
- 8. Similarly, Renee R. "An overview on the use of titanium in the aerospace industry." Materials Science and Engineering: A 213.1-2 (1996): 103-114. doi:10.1016/0921-5093(96)10233-1
- 9. Kasprzak, Wojciech, BabakShalchiAmirkhiz, and Marek Niewczas. "Structure and properties of cast Al–Si based alloy with Zr–V–Ti additions and its evaluation of high temperature performance." Journal of Alloys and Compounds 595 (2014): 67-79. doi: 10.1016/j.jallcom.2013.11.209
- 10. Zeren, Muzaffer, and ErdemKarakulak. "Influence of Ti addition on the microstructure and hardness properties of near-eutectic Al–Si alloys." Journal of Alloys and Compounds 450.1-2 (2008): 255-259. doi: 10.1016/j. jallcom.2006.10.131
- 11. Ahmed, E. M. "Physical properties of as melt spun Al–7 wt.% Si–x wt.% Ti." Materials Letters 62.6-7 (2008): 960-963. doi: 10.1016/j.matlet.2007.07.040
- 12. Ghomashchi, Reza. The evolution of AlTiSi intermetallic phases in Ti-added A356 Al–Si alloy. Journal of Alloys and Compounds 537 (2012): 255-260. doi: 10.1016/j.jallcom.2012.04.087
- 13. Zeren, Muzaffer, and ErdemKarakulak. Influence of Ti addition on the microstructure and hardness properties of near-eutectic Al–Si alloys. Journal of Alloys and Compounds 450.1-2 (2008): 255-259. doi: 10.1016/j. jallcom.2006.10.131

- 14. Gao, Tong, et al. "Influence of Si and Ti contents on the microstructure, microhardness and performance of TiAlSi intermetallics in Al–Si–Ti alloys." Journal of Alloys and Compounds 509.31 (2011): 8013-8017. doi:10.1016/j.jallcom.2011.05.032
- 15. Saheb, N., et al. "Influence of Ti addition on wear properties of Al–Si eutectic alloys." Wear 249.8 (2001): 656-662. doi:10.1016/s0043-1648(01)00687-1
- 16. Xie, Jing Pei, et al. "Investigation on wear resistance of Al-Si-Ti piston alloys produced by electrolysis." Materials science forum. Vol. 546. Trans Tech Publications Ltd, 2007. doi:10.4028/www.scientific.net/msf.546-549.905.
- 17. Subhi, AkeelDhahir, Ali AbbarKhleif, and QasimSaad Abdul-Wahid. "Microstructural investigation and wear characteristics of Al-Si-Ti cast alloys." Engineering Transactions 68.4 (2020): 385-395. doi: 10. 24423/EngTrans.1156.20201029
- 18. Kim, K. Y., and W. R. Marshall Jr. "Drop-size distributions from pneumatic atomizers." AIChE Journal 17.3 (1971): 575-584.
- 19. Srivastava, V. C., R. K. Mandal, and S. N_ Ojha. "Microstructure and mechanical properties of Al-Si alloys produced by spray forming process." Materials Science and Engineering: A 304 (2001): 555-558.
- 20. Lavernia, Enrique J., and Yue Wu. "Spray atomization and deposition." (No Title) (1996). pp 487-489
- 21. Grant, P. S. "Spray forming." Progress in Materials science 39.4-5 (1995): 497-545.
- 22. Gupta, Shant Prakash. "Intermetallic compounds in diffusion couples of Ti with an Al–Si eutectic alloy." Materials Characterization 49.4 (2002): 321-330. doi: 10.1016/S1044-5803(02)00342-X
- 23. Niu, Yingshuo, et al. "Microstructure, mechanical properties and wear behavior of Al–20Si–3Fe alloy prepared by spray Conform." Materials Research Express 6.8 (2019): 086578. doi: 10.1088/2053-1591/ab1d15
- 24. Venkataraman Reddy, Bandi, et al. "Enhancement of microstructure and mechanical performance of spray formed Al-6Si-18Pb alloy by warm rolling." Advances in Materials and Processing Technologies 8.sup4 (2022): 2262-2276. doi: 10.1080/2374068X.2022.2036490
- 25. Raju, K., S. N. Ojha, and A. P. Harsha. "Spray forming of aluminum alloys and its composites: an overview." Journal of materials science 43.8 (2008): 2509-2521. doi: 10.1007/s10853-008-2464-x
- 26. Shen, Xiao, et al. "Effect of cooling rate on the microstructure evolution and mechanical properties of Iron-Rich Al–Si Alloy." Materials 15.2 (2022): 411. doi: 10.3390/ma15020411
- 27. Anand, S., et al. "Processing, microstructure and fracture behavior of a spray atomized and deposited aluminum–silicon alloy." Journal of Materials Science 32 (1997): 2835-2848.
- 28. Raju, K., A. P. Harsha, and S. N. Ojha. "Microstructural Features, Wear, and Corrosion Behavior of Spray Cast Al—Si Alloys." Proceedings of the Institution of Mechanical Engineers, Part J: Journal of Engineering Tribology 225.3 (2011): 151-160.
- 29. Bubenkó, Marianna, et al. "The Effect of the Excess Titanium Content on the Microstructure of Al–Si Foundry Alloys." International Journal of Engineering and Management Sciences 4.1 (2019): 12-20. DOI:10.21791/IJEMS.2019.1.2.
- 30. Chen, X-G., and M. Fortier. "TiAlSi intermetallic formation and its impact on the casting processing in Al–Si alloys." Journal of Materials Processing Technology 210.13 (2010): 1780-1786. doi: 10.1016/j.jmatprotec.2010.06.009

- 31. Javidani, Mousa, and Daniel Larouche. "Application of cast Al–Si alloys in internal combustion engine components." International Materials Reviews 59.3 (2014): 132-158. doi:10.1179/1743280413y.0000000027
- 32. Esmeralda, A. G., et al. "Thermal diffusivity of Al-Si cast alloys for internal combustion engines." Thermochemical acta 675 (2019): 172-179. doi: 10.1016/j.tca.2019.03.020
- 33. Otarawanna, S., and A. K. Dahle. "Casting of aluminum alloys." Fundamentals of aluminum metallurgy. Woodhead Publishing, 2011. 141-154. doi:10.1533/9780857090256.1.141
- 34. Dunstan, D. J., and A. J. Bushby. "Grain size dependence of the strength of metals: The Hall—Petch effect does not scale as the inverse square root of grain size." International Journal of Plasticity 53 (2014): 56-65. doi: 10.1016/j.ijplas.2013.07.004
- 35. Ma, X., et al,. "Temperature-dependent hardness of metals: A review." Journal of Materials Science, 55(10). (2020): 7411-7433.doi: 10.1007/s10853-020-04523-8
- 36. Kumar, S., et al. "Wear behavior of Al-15Si-2Ti alloy at elevated temperatures." Wear, 376-377(2017):1132-1140.
- 37. Liu, H., et al."High-temperature wear behavior of Al-Si-Ti alloys."Tribology International.81(2015): 301-308. doi: 10.1016/j.triboint.2014.09.014
- 38. Zhang, Y., et al. "Strain hardening behavior of Al-15Si-2Ti alloy during high-temperature wear." Wear, 410-411(2018): 12-20.doi 10.1016/j.wear.2018.05.015
- 39. Zhang, J., et al."High-temperature wear behavior of Al-Si alloys: Effect of thermal activation of plastic deformation mechanisms."Wear.432-433(2019):102945. doi: 10.1016/j.wear.2019.102945
- 40. Torres, Hector, Markus Varga, and M. Rodríguez Ripoll. "High temperature hardness of steels and iron-based alloys." Materials Science and Engineering: A 671 (2016): 170-181. doi: 10.1016/j.msea.2016.06.058
- 41. Yang, L. J. "Wear coefficient equation for aluminum-based matrix composites against steel disc." Wear 255.1-6 (2003): 579-592. https://doi.org/10.1016/S0043-1648(03)00191-1
- 42. Lim, S. C., et al. "Wear of a spray-deposited hypereutectic aluminum-silicon alloy." Journal of materials processing technology 63.1-3 (1997): 865-870. https://doi.org/10.1016/S0924-0136(96)02740-9
- 43. Hogmark, S., S. Jacobson, and O. Vingsbo. "ASM Handbook on Friction, Lubrication and Wear Technology." Blau, P. (Ed.) 18 (1992): 176-183.
- 44. Lim, S. C., & Ashby, M. F. (1987). "Wear mechanism maps." Acta Metallurgica, 35(1)(1987) 1-24.doi:10.1016/0001-6160(87)90002-5
- 45. Bai, BN Pramila, and S. K. Biswas. "Characterization of dry sliding wear of Al-Si alloys." Wear 120.1 (1987): 61-74. https://doi.org/10.1016/0043-1648(87)90133-5
- 46. Zhang, J. "Wear debris formation and its relationship with material properties." Wear, 410-411(2018): 21-31.doi: 10.1016/j.wear.2018.05.017
- 47. Das, S., S. V. Prasad, and T. R. Ramachandran."Microstructure and wear of cast (Al-Si alloy)-graphite composites. Wear 133.1(1989):173-187.https://doi.org/10.1016/0043-1648(89)90122-1
- 48. Zhang, J. "Wear mechanisms and classification." In "Wear of Materials".(2018): 1-14). doi: 10.1016/B978-0-12-812810-8.00001-6